PNL-3374
UC-94e

# Analytical Modeling of a Hydraulically-Compensated Compressed Air Energy Storage System

C. A. McMonagle
D. S. Rowe

December 1982

Prepared for Pacific Northwest Laboratory
under Agreement B-43388-A-L
for the U.S. Department of Energy
under Contract DE-AC06-76RLO 1830

Pacific Northwest Laboratory
Operated for the U.S. Department of Energy
by Battelle Memorial Institute

PNL-3374

## DISCLAIMER



PACIFIC NORTHWEST LABORATORY
*operated by*
BATTELLE
*for the*
UNITED STATES DEPARTMENT OF ENERGY
*under Contract DE-AC06-76RLO 1830*

Printed in the United States of America
Available from
National Technical Information Service
United States Department of Commerce
5285 Port Royal Road
Springfield, Virginia 22151

NTIS Price Codes
Microfiche A01

Printed Copy

| Pages | Price Codes |
|---|---|
| 001-025 | A02 |
| 026-050 | A03 |
| 051-075 | A04 |
| 076-100 | A05 |
| 101-125 | A06 |
| 126-150 | A07 |
| 151-175 | A08 |
| 176-200 | A09 |
| 201-225 | A010 |
| 226-250 | A011 |
| 251-275 | A012 |
| 276-300 | A013 |

PNL-3374
UC-94e



# ANALYTICAL MODELING OF A HYDRAULICALLY-COMPENSATED COMPRESSED AIR ENERGY STORAGE SYSTEM

C. A. McMonagle
D. S. Rowe
Rowe & Associates, Inc.

December 1982

Prepared for
the U.S. Department of Energy
under Contract DE-AC06-76RLO 1830

Pacific Northwest Laboratory
Richland, Washington 99352

## FOREWORD

Compressed air energy storage (CAES) is a technique for supplying electric power to meet peak load requirements of electric utility systems. Using low-cost power from base load plants during off-peak periods, a CAES plant compresses air for storage in an underground reservoir--an aquifer, solution-mined salt cavity, or mined hard rock cavern. During subsequent peak load periods, the compressed air is withdrawn from storage, heated, and expanded through turbines to generate peak power. This relatively new technology offers significant potential for reducing costs and improving efficiency of electric power generation, as well as reducing petroleum fuel consumption.

Based on these potential benefits, the U.S. Department of Energy (DOE) is sponsoring a comprehensive program to accelerate commercialization of CAES technology. The Pacific Northwest Laboratory (PNL) was designated the lead laboratory for the CAES Program. As such, PNL is responsible for assisting the DOE in planning, budgeting, contracting, managing, reporting, and disseminating information. Under subcontract to PNL are a number of companies, universities, and consultants responsible for various research tasks within the program.

An important element of this program is to investigate phenomena that may be detrimental in the commercialization of CAES. One such concern is the "champagne effect". It is thought that the champagne effect may occur in a hydraulically-compensated hard rock cavern when air, dissolved in the water by diffusion through the air-water interface, rises to the surface with an increasing air volume fraction due to deaeration of water and decompression of the air in the decreasing pressure field. This process has the potential to cause a loss of cavern pressure or even blowout of the cavern. This report presents and applies an analytical model developed by Rowe & Associates, Inc., that can calculate the dynamic behavior of a hydraulically-compensated CAES system. In using this model, it has been determined that the champagne effect is unlikely to cause significant problems for a properly designed CAES system.

Other than comparison to Helmholtz oscillators there was no attempt to validate the model predictions. The reason for this is that there is virtually no data available relevant to operation of compensated hard rock CAES reservoirs under the conditions simulated. Data has been gathered in an 18 bar facility in Luxembourg; however, that data is unavailable to U.S. researchers. Physical modeling studies are currently underway at Rensselaer Polytechnic Institute and this data will be available at a later date. Furthermore, the Electric Power Research Institute is supporting research which will better define physical processes germain to the "champagne effect" at pressures up to 80 bar. Once these data becomes available, validation of the computer model and its predictions can be performed. However, until that time, the results here serve to characterize reservoir behavior under conditions and assumptions thought to be conservative in the sense that the predicted "champagne effect" will be more severe than might be realistically expected.

## SUMMARY

A computer program was developed to calculate the dynamic response of a hydraulically-compensated compressed air energy storage (CAES) system, including the compressor, air pipe, cavern, and hydraulic compensation pipe. The model is theoretically based on the "two-fluid" model in which the dynamics of each phase are presented by its set of conservation equations for mass and momentum. The conservation equations define the space and time distribution of pressure, void fraction, air saturation, and phase velocities. The phases are coupled by two interface equations. The first defines the rate of generation (or dissolution) of gaseous air in water and can include the effects of supersaturation. The second defines the frictional shear coupling (drag) between the gaseous air and water as they move relative to each other. The relative motion of the air and water is, therefore, calculated and not specified by a slip or drift-velocity correlation.

The total CAES system is represented by a nodal arrangement. The nodal sizes are arbitrary, but require the assumption of one-dimensional flow. The conservation equations are written for each nodal volume and are solved numerically. System boundary conditions include the air flow rate (defined by compressor characteristics), atmospheric pressure at the top of the compensation pipe, and air saturation in the reservoir. Initial conditions are selected for velocity and air saturation. Uniform and constant temperature (60°F) is assumed. The equations are solved numerically by a digital computer.

The analytical model was used to investigate the dynamic response of the proposed Potomac Electric Power Company (PEPCO) system being designed by Acres American. Investigative calculations considered high and low water levels, fully and partially air-saturated water as an initial condition, a variety of air-charging rates, modifications to the functional form of the air source, and a range of wall and interfacial friction factors.

For all cases investigated, the cavern response to air-charging was a damped oscillation of pressure and flow. Detailed results are presented for a low water level initial condition, representative of a "worst-case" charging cycle. These conservatively oriented calculations indicate that the Champagne Effect is unlikely to cause blowout for a properly designed CAES system.

CONTENTS

# NOMENCLATURE

Alphabetic:

| | |
|---|---|
| $A$ | cross section flow area |
| $C$ | mass fraction of dissolved air |
| $C_b$ | bubble drag coefficient |
| $D$ | diameter |
| $D_b$ | bubble diameter |
| $f$ | friction factor |
| $g$ | gravity |
| $H$ | Henry's law constant |
| $K_g$ | rate constant for air source |
| $K_i$ | interfacial shear coefficient |
| $M$ | molecular weight |
| $P$ | pressure |
| $R$ | universal gas constant |
| $R_e$ | Reynolds number |
| $S_g$ | air source |
| $t$ | time |
| $T_o$ | reference temperature |
| $u$ | velocity |
| $V$ | volume |
| $V_c$ | volume of continuity cell |
| $V_m$ | volume of momentum cell |
| $W_e$ | Weber number |
| $x$ | distance |

Greek:

| | |
|---|---|
| $\alpha$ | void fraction |
| $\rho$ | density |
| $\tau$ | shear |
| $\mu$ | viscosity |

Subscripts:

| | |
|---|---|
| g | air as a gas |
| l | liquid water |
| a | air dissolved in water |
| j | node location |
| sat | saturated air |

# Section I
# INTRODUCTION

Hydraulically-compensated caverns are being considered for compressed air energy storage (CAES) applications. In this concept, high pressure air is stored in a deep mined cavern; the pressure is maintained by the hydrostatic heat from a surface reservoir adjacent to the cavern. Water in the cavern is displaced to the reservoir during energy storage periods. The water reenters the cavern as air is fed to a gas turbine during energy withdrawal.

During the air storage period, air dissolves in the water by diffusion through the air-water interface. Although this process is slow, the impact of fully air-saturated water could be a problem. As air-saturated water flows up the compensation pipe to the reservoir, the pressure would decrease and the air would come out of solution to form bubbles (Champagne Effect). This two-phase air-water mixture would flow to the surface with an increasing air volume fraction due to deaeration and decompression of the air in the decreasing pressure field. The net result would be a reduced hydrostatic head on the cavern, which could drive the flow even faster. Further, the flow could be unstable, resulting in loss of cavern pressure and eventual blowout. This could, in turn, lead to loss of substantial energy and possibly cause property damage and personal injury.

Previous analyses have identified the nature of the Champagne Effect problem[1,2,8]. Although they provide important insight, these previous studies have generally been limited to a consideration of the separate effects or have used rather simplified models for two-phase flow. The dynamic behavior of the two-phase flow still required more comprehensive description.

In response to this need, Rowe & Associates, Inc., subcontracted with the Pacific Northwest Laboratory (PNL) to develop an analytical model capable of fully describing the dynamic behavior of a

hydraulically-compensated CAES system. The resulting model, documented in this report, also includes the space and time distribution of air saturation, void fraction, pressure, and fluid velocity. The model also considers other effects of importance to cavern analysis, including relative phase motion of the system's air and water, and supersaturation.

This report presents the theoretical basis, solution method, and verification of the model. Results of an analysis using the model are also presented. A complete description of, and user instructions for, the model are appended to the report.

## Section II
## CONCLUSIONS

The analytical model provides a theoretical basis and computational procedure to calculate the dynamic response of the compressed air energy storage system including the compressor, air pipe, cavern, and hydraulic compensation pipe.

The analytical model has been used to investigate the dynamic response of the proposed Potomac Electric Power Company (PEPCO) CAES system. Calculations performed on the proposed PEPCO system design showed that, for all air-charging rates considered, the cavern response was a damped oscillation of the pressure and flow. Results of model calculations suggest that certain variations in system parameters will reduce the Champagne Effect:

- design parameters
  - include deep surface reservoir
  - provide cavern bottom contouring
  - modify design (not yet considered): e.g., U-bend, flow-restricting orifice, pipe diameter
- operational parameters
  - reduce compressor start-up rate
  - reduce compressor flow rate
  - impede air dissolution rate
  - charge from high water level
- correlation parameters
  - increased wall friction
  - reduced interfacial friction
  - model nonequilibrium air source.

Results for a low water level initial condition, representative of a "worst case" charging cycle, indicate that the Champagne Effect is unlikely to cause blowout for a properly designed CAES system.

## Section III

## ANALYTICAL MODEL

This section presents the theoretical basis for the analytical model including the conservation equations of mass and momentum and the constitutive equations for closure. The theoretical model is adapted from the "two-fluid" modelling philosophy which has emerged as a current state-of-the-art approach for considering two phase flow[4,5]. The basic approach is to write the conservation equations for each phase, and then to couple them by interface equations (jump conditions). The methodology has had considerable success for complex two-phase flow situations in nuclear reactor safety technology[4].

### CONSERVATION EQUATIONS

Equations describing the conservation of mass and momentum for the air, liquid and dissolved air are used to calculate the thermal-hydraulic response of the compressed air storage facility as a function of time. The equations are presented for one-dimensional flow which is assumed for the analysis.

### Conservation of Mass

The mass conservation equations, in differential form, for the three-constituents of the flow are:

for the gas,

$$\frac{\partial}{\partial t}\alpha_g\rho_g + \frac{\partial}{\partial x}\alpha_g\rho_g U_g = S_g \qquad (3.1)$$

for the liquid,

$$\frac{\partial}{\partial t}\alpha_\ell\rho_\ell + \frac{\partial}{\partial x}\alpha_\ell\rho_\ell U_\ell = 0 \qquad (3.2)$$

and for the dissolved air,

$$\frac{\partial}{\partial t}\alpha_a\rho_a^* + \frac{\partial}{\partial x}\alpha_a\rho_a^* U_a = -S_g \qquad (3.3)$$

Where void fractions ($\alpha$), densities ($\rho$) and velocities ($U$) are each subscripted $\ell$, a or g to represent liquid, dissolved air and gas, respectively. The air source, $S_g$, couples the two air fields and can model both dissolution and deaeration.

Assuming $U_s = U_\ell$, $\alpha_a = 0$ and that the volume of liquid does not change with the amount of dissolved air, $\partial\rho_\ell/\partial\rho_a = 0$, Equation (3.3) can be written as

$$\frac{\partial}{\partial t}\alpha_\ell\rho_a + \frac{\partial}{\partial x}\alpha_\ell\rho U_{a\,\ell} = -S_g \qquad (3.4)$$

where $$\rho_a = \frac{\text{lb dissolved air}}{\text{ft}^3 \text{ liquid}}$$

Equations (3.1, (3.2) and (3.4) are the phase mass conservation equations used in this analysis. These equations define the space and time mass distributions of air, liquid and dissolved air as a function of their repspective mass flow rates and the air source.

Conservation of Momentum

The momentum equations are:

for air as a gas,

$$\frac{\partial}{\partial t}\alpha_g\rho_g U_g + \frac{\partial}{\partial x}\alpha_g\rho_g U_g^2 = -\alpha_g\frac{\partial P}{\partial x} + g\,\alpha_g\rho_g - \tau_{wg} - \tau_{\ell g} - \tau_{ag} + S_g U_a \qquad (3.5)$$

for liquid,

$$\frac{\partial}{\partial t}\alpha_\ell\rho_\ell U_\ell + \frac{\partial}{\partial x}\alpha_\ell\rho_\ell U_\ell^2 = -\alpha_\ell\frac{\partial P}{\partial x} + g\,\alpha_\ell\rho_\ell - \tau_{w\ell} + \tau_{\ell g} + \tau_{\ell a} \qquad (3.6)$$

and for dissolved air,

$$\frac{\partial}{\partial t}\alpha_a\rho_a^* U_a + \frac{\partial}{\partial x}\alpha_a\rho_a^* U_a^2 = -\alpha\frac{\partial P}{\partial x} + g\,\alpha_a\rho_a^* - \tau_{aw} - \tau_{\ell a} - S_g U_a + \tau_{ag} \tag{3.7}$$

Surface tension forces are not included because the pressure is assumed equal for all phases. Shear forces are defined as: $\tau_{wg}$, between the wall and the gas, $\tau_{w\ell}$, between the wall and the liquid, $\tau_{wa}$, between the wall and the dissolved air, $\tau_{\ell g}$, between the gas and the liquid, $\tau_{\ell a}$, between the liquid and the dissolved air, and $\tau_{ga}$, between the gas and the dissolved air. It should be noted that the equations are coupled by interfacial shear and by the air source momentum exchange ($S_g U_a$).

Equations (3.6) and (3.7) are added to provide a mixture momentum equation for the liquid and dissolved air. Applying the same assumptions as before ($U_a = U_\ell$, $\alpha_a = 0$, $\partial\rho_\ell/\partial\rho_a = 0$), the result is

$$\frac{\partial}{\partial t}(\rho_\ell + \rho_a)\,\alpha_\ell U_\ell + \frac{\partial}{\partial x}\alpha_\ell(\rho_\ell + \rho_a)U_\ell^2 = -\alpha_\ell\frac{\partial P}{\partial x} + g\,\alpha_\ell(\rho_\ell + \rho_a) + \tau_{\ell g} - \tau_{w\ell} - S_g U_\ell \tag{3.8}$$

Details of the solution make it convenient to convert the conservative form of the momentum equations to the transportive form. For air as a gas, this is accomplished by multiplying the vapor continuity equation by $U_g$ and subtracting the result from Equation (3.5). For the dissolved air and liquid mixture, it is accomplished by subtracting the liquid and dissolved air continuity equations multiplied by $U_1$ from Equation (3.8). The resulting momentum equations are:

for air as a gas,

$$\alpha_g\rho_g\frac{\partial}{\partial t}U_g + \alpha\rho_g U_g\frac{\partial}{\partial x}U_g = -\alpha_g\frac{\partial}{\partial x}P + g\,\alpha_g\rho_g - \tau_{wg} - \tau_{\ell g} + S_g U_\ell - S_g U_g \tag{3.9}$$

and for the liquid-dissolved air mixture,

$$\alpha_\ell \rho_\ell \frac{\partial}{\partial t} U_\ell + \alpha_\ell \rho_\ell U_\ell \frac{\partial}{\partial x} U_\ell = - \alpha_\ell \frac{\partial P}{\partial x} + g \alpha_\ell \rho_\ell + \tau_{\ell g} - \tau_{w\ell} \qquad (3.10)$$

In this final step it has been assumed that the dissolved air/gas interfacial shear, $\tau_{ag}$, is insignificant and it has been neglected in Equation (3.9), and that the contribution of $\rho_a$ in the liquid/dissolved air mixture momentum equation is insignificant with respect to $\rho_l$ ( $\frac{\rho a}{\rho l} < .002$ for typical design conditions) and $\rho_a$ has therefore been neglected in Equation (3.10).

Conservation of Energy

It is presently assumed that the system operates at constant temperature (60° F in the sample calculations); therefore, the liquid and vapor energy equations are not explicitly solved. While this approximation would likely have little effect on the liquid phase calculations, it could significantly affect the gas phase results due to the linear temperature--specific volume relationship of the gas.

Assuming air behaved as a polytropic gas, Mollendorf[1] compared gas decompression for the adiabatic and isothermal cases and demonstrated that the isothermal case represents a worst case approximation as it concerns the Champagne Effect because gas density and total hydrostatic head in the compensation pipe are minimum for the isothermal approximation. An analogous argument can also be made for gas within the cavern; however, the effect is less here because the cavern pressure change is only a few psia whereas the pressure change for bubbles rising from the bottom to the top of the compensation pipe can be as large as 1000 psia.

The isothermal approximation is therefore consistent with the desire to provide a conservative estimate of the Champagne Effect. Alternatively, the isothermal result could be achieved by including the gas and liquid energy equations in the analytical model and assume large heat transfer rates to force uniform temperatures.

The energy equations have not been included in the current model because doing so would introduce additional calculation time to solve the equation set and because the isothermal case is expected to yield the most conservative results. It is possible however to refine the solution algorithm to include temperature changes, and this might be a valuable addition at a later date to allow best estimate calculations versus the conservatively oriented approach in the present model.

## CONSTITUTIVE EQUATIONS

The conservation equations require equations of state for the liquid and vapor densities and for the saturation concentration of dissolved air. Interfacial shear, wall shear, and the air source must also be specified for closure.

### Equations of State

Equations of state are required to define the density of the three constituents. The equations are:

$$\rho_\ell = \rho_\ell\,(To) \tag{3.11}$$

$$\rho_g = P\,M_g/RTo \tag{3.12}$$

$$\rho_{a_{sat}} = \frac{P}{H(To,P)}\,\rho_\ell M_g/M_\ell \tag{3.13}$$

where a constant temperature ($T_o$) has been assumed. The liquid is assumed to be incompressible, thus, the density is constant and defined at constant temperature ($T_o$). The gas density is defined by the perfect gas law where $M_g$ is the molecular weight of air (28.97) and R is the universal gas constant. The density of dissolved air, defined as the mass of dissolved air per unit volume of water is defined by Henry's law for solubility[6]. The Henry's law constant is actually a function of pressure and temperature. The values of H used in the analysis are shown in Figure III-1. Values of H at atmospheric pressure are available in Perry's Handbook (pg. 3-96)[6]. The pressure variation of H is given by[7]

$$H\,(To,P) = H\,(To,1) + 433.8\,(P-1) \tag{3.14}$$

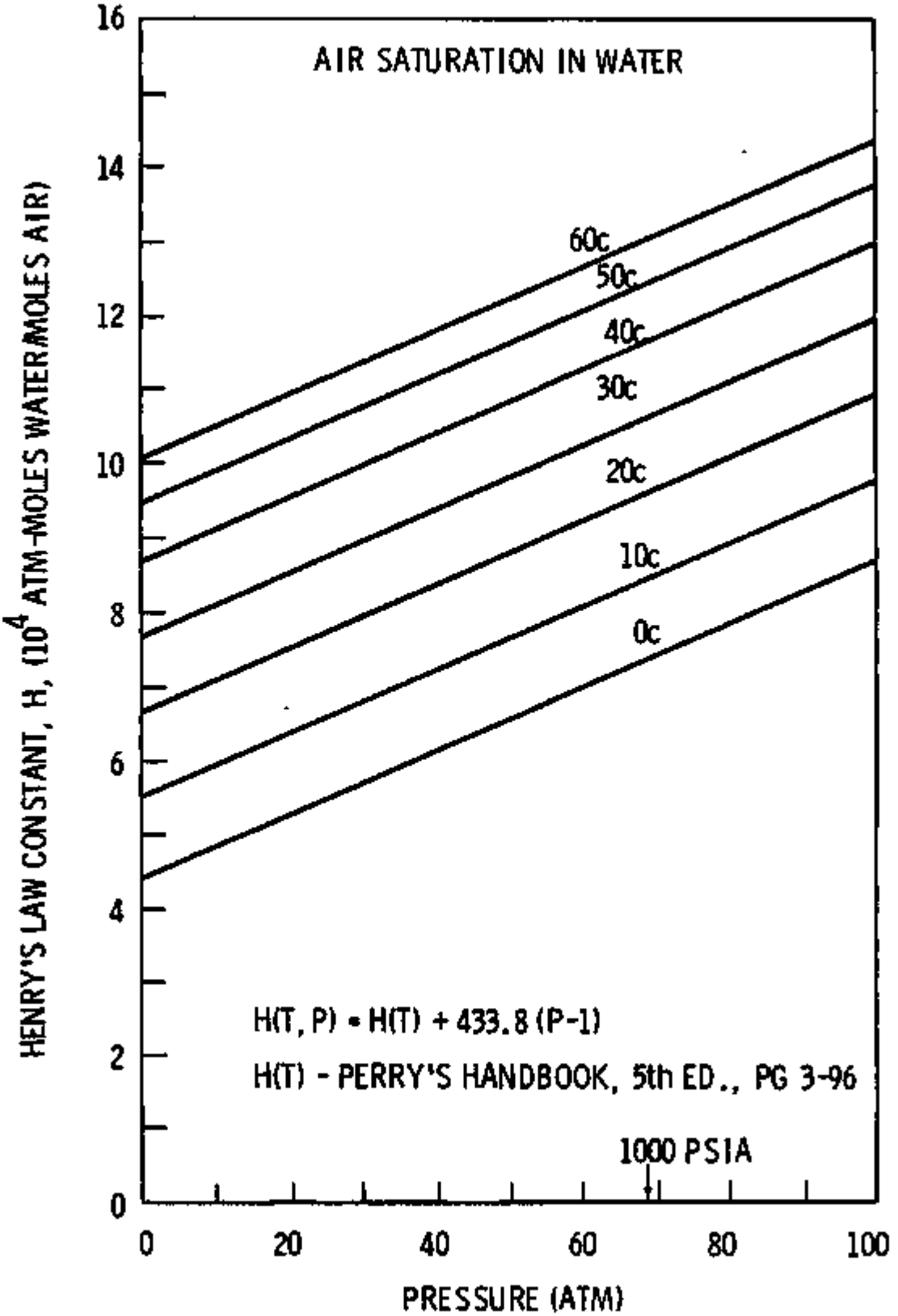


Figure III-1. Henry's Law Constant for Saturation.

where P is the pressure in atmospheres and the units of H are atm-moles water/moles air.

The mass fraction of air dissolved in water by Henry's law (Perry, pg. 14-3) is

$$C = \frac{P}{H(To,P)} \frac{M_g}{M_\ell} \tag{3.15}$$

where $M_g$ and $M_l$ are the molecular weights of air and water, respectively.

Figure III-2 presents a plot of the air saturation as a function of temperature and pressure[7]. It is obtained from the values of H in Figure III-1 and is derived from the equation

$$(V_g/V_\ell)_{P=1} = \frac{P}{H(To,P)} (M_g/M_\ell) (\rho_\ell/\rho_g)_{P=1} \tag{3.16}$$

Note that for a saturation pressure of about 65 atm, the volume of air is about the same as the volume of water. This translates to a void fraction of 0.5 or less when fully saturated cavern water at 65 atm undergoes decompression to 1 atm. Void fractions in the compensation pipe would be much lower than this because of hydrostatic compression. Void fractions of this magnitude indicate bubbly flow. Slug flow behavior is unlikely.

Air Source

The functional form for the air source is assumed to be

$$S_g = K_g (1-\alpha) (\rho_a - \rho_{a_{sat}}) \tag{3.17}$$

where

$$K_g = \begin{cases} 10^4 & ; \ \rho_a - \rho_{a_{sat}} > 0 \\ 0 & ; \ \rho_a - \rho_{a_{sat}} < 0 \end{cases} \tag{3.18}$$

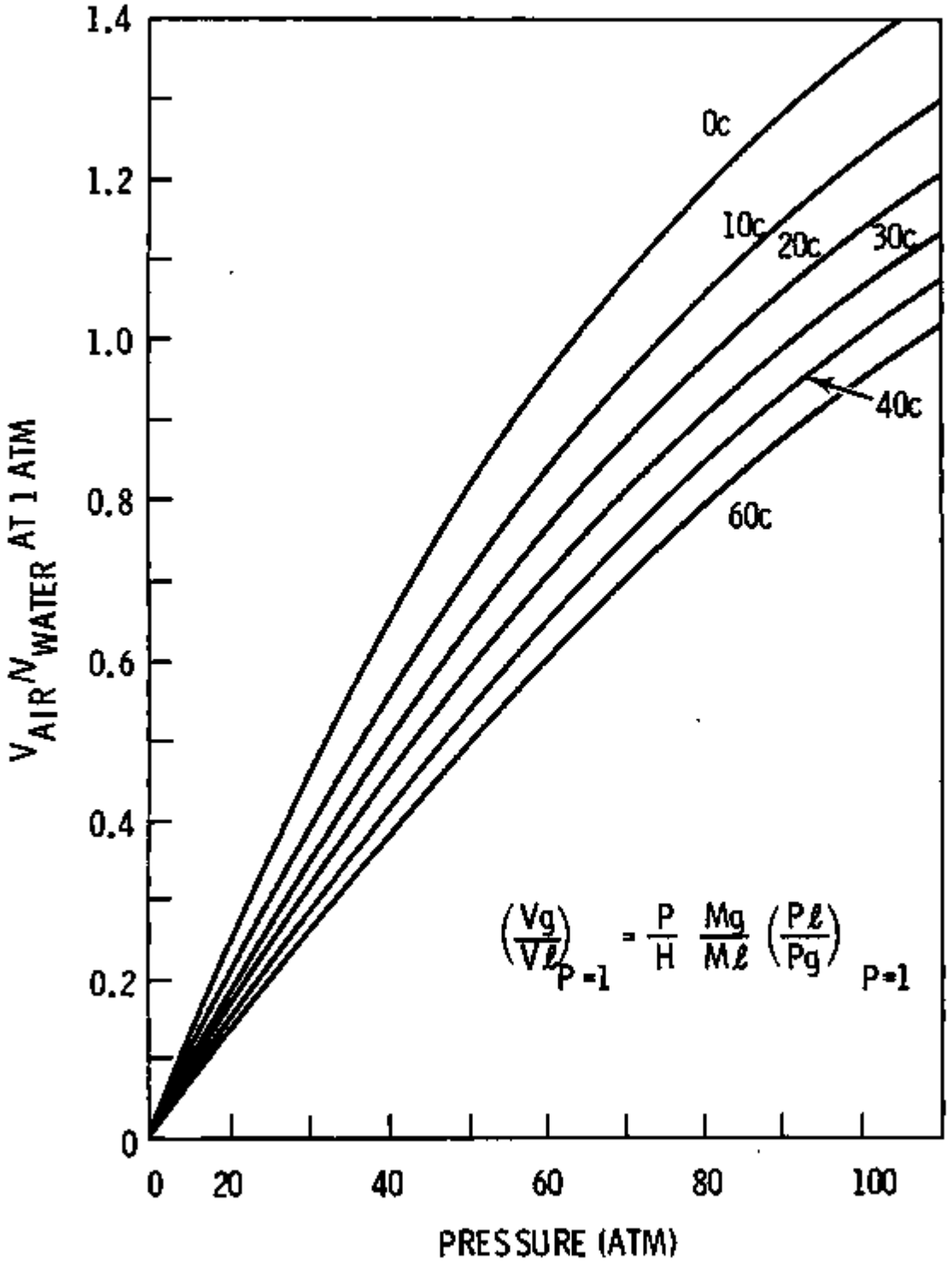


Figure III-2. Volume Fraction of Air Dissolved in Water As A Function of Pressure and Temperature.

The assumed coefficients ($K_g$) force the dissolved air to be released at nearly equilibrium, but will not allow air to reenter the water should the dissolved air concentration fall below the saturation value.

The general form of the air source is important because theoretically or experimentally determined values of $K_g$ may be easily incorporated into the model at any time. The values shown here force a large amount of gaseous air to be present at any time and provide an upper bound for the rate process.

Delayed nucleation and oversaturation can be modeled by requiring a defined threshold. In that case, $K_g$ would be zero until $\rho_a - \rho_{aSAT} > \delta\rho$ where $\delta\rho$ is the oversaturation threshold. The rate process of nucleation can be modeled through the value of $K_g$. Comparative calculations have investigated the consequences of reducing $K_g$ to force lesser amounts of air release and of incorporating delayed nucleation. For the cases investigated, the most conservative results are obtained using an air source which allows the maximum amount of air release from the liquid.

Interfacial Shear

Interfacial shear is postulated to be of the form

$$\tau_{g\ell} = K_i |U_r| U_r \tag{3.19}$$

As previously discussed, the void fractions are relatively low in most CAES applications, therefore, the bubbly flow regime is appropriate and the bubble drag coefficient, $K_i$, is given by[4]

$$K_i = C_b \frac{\alpha\rho_\ell}{2D_b} \tag{3.20}$$

The bubble diameter, $D_b$, is selected based on a critical Weber number of 25[4], therefore,

$$D_b = (W_{b_{crit}} \sigma) / (\rho_\ell U_r^2) \tag{3.21}$$

The coefficient, $C_b$ is selected based on the bubble Reynolds number and is defined by[4]

$$C_b = \begin{bmatrix} 240. & ; & Re_b < .1 \\ 24.0 / Re_b & ; & .01 \leq 2.0 \\ 18.7 / Re_b & ; & Re_b > 2.0 \end{bmatrix} \tag{3.22}$$

where

$$Re_b = \rho_\ell U_r D_b / \mu_\ell \tag{3.23}$$

For $\alpha > .999$ and $\alpha < .001$, $C_b$ is set to a large number to force equal velocities in these cases.

The relative velocity, $U_r$, is defined as

$$U_r = U_g - U_\ell - \frac{(Co-1)}{(1-\alpha_d)} j \tag{3.24}$$

where $\alpha_d$ is the volume fraction of the dispersed phase. This definition of the relative velocity has been offered by Ishii and Chawla[10] to account for phase distribution effects across the pipe cross-section. Equation (3.24) can be simplified by introducing the definition of the volumetric flux, j,

$$j = \alpha U_g + (1-\alpha) U_\ell \tag{3.25}$$

to obtain

$$U_r = \left\{ 1 - \frac{\alpha(Co-1)}{(1-\alpha_d)} \right\} U_g - \left\{ 1 + (1-\alpha) \frac{(Co-1)}{(1-\alpha_d)} \right\} U_\ell \tag{3.26}$$

It is convenient to define the relative velocity as

$$U_r = Co_v U_g - Co_\ell U_\ell \tag{3.27}$$

where $C_{ov}$ and $C_{ol}$ follow immediately from Equation (3.26).

The phase distribution parameter, $C_o$, is defined as

$$C_o = \frac{\langle \alpha j \rangle}{\langle j \rangle \langle \alpha \rangle} \tag{3.28}$$

where the brackets, $\langle\ \rangle$, are used to define area averaged values. The distribution parameter equals 1.0 for uniform distributions of velocity and void fraction. For developed bubbly flow in a pipe, bubbles tend to position in the higher velocity, central region and $C_o$ is then greater than 1.0. The effects of $C_o$ can be illustrated by comparing two cases. The first is for $C_o$ = 1.0, uniform profiles, for which the relative velocity as defined by Equation (3.26) becomes $U_r = U_g - U_l$. The second case is $C_o > 1.0$ and, for $U_g$ and $U_l$ positive, phase distribution effects reduce the relative velocity and hence reduce the interfacial shear for given $U_g$ and $U_l$.

Comparative calculations in CAES have demonstrated that $C_o > 1.0$ results in a reduction of Champagne Effect induced oscillations because calculated values of $U_g - U_l$ are greater that that using $C_o$ = 1.0 and more vapor consequently escapes from the compensation pipe. Therefore, the conservatively oriented calculations provided here use $C_o$ = 1.0.

Wall Shear

Wall shear is treated in the standard manner by assuming

$$\tau_{wk} = \tfrac{1}{2} \left\{ \frac{f}{D} + \frac{C_d}{\Delta x} \right\} (\alpha\rho)_k \, |U_k| \, U_k \tag{3.29}$$

where the subscript, k, is used to denote either the liquid or gas phase. $C_d$ is a loss coefficient used to represent orifices and other sources of nonrecoverable losses. Unless otherwise stated, $C_d$ = 0.0, in the reported calculations. The friction factor, f, is presently evaluated using a standard tube correlation,

$$f = \text{MAX} \{ a\ Re^{-b} + c,\ d \} \tag{3.30}$$

where

$$R_e = |(\rho u)\, D/\mu| \tag{3.31}$$

$$a = .316 \tag{3.32}$$

$$b = -.25 \tag{3.33}$$

$$c = 0.0 \tag{3.34}$$

$$d = .015 \tag{3.35}$$

$$(\rho u) = \alpha_g \rho_g U_g + \alpha_\ell \rho_\ell U_\ell \tag{3.36}$$

$$\mu = \left\{ \frac{X}{\mu_g} + \frac{1-X}{\mu_\ell} \right\}^{-1} \tag{3.37}$$

$$X = |\alpha_g \rho_g U_g| / |(\rho u)| \tag{3.38}$$

This correlation represents the homogeneous friction model when $U_g = U_l$, which it need not in this analysis. However, this model was selected because the homogeneous correlation generally provides a smaller value for friction factor at the void fractions of interest in comparison to many other commonly applied correlations. This choice is therefore consistent with the conservative orientation of the model because reduced friction accentuates the Champagne Effect.

## Section IV

## SOLUTION METHOD

There are two parts to the development of the solution process. The first is the establishment of an equation set which describes the phenomena of interest, and the second is the use of an applicable solution algorithm to solve the chosen equation set.

A finite difference numerical method is used to solve the equations of the previous section. The CAES system is represented by a number of connected control volumes or, as they are interchangably called, finite difference cells with the finite difference method. Each control volume simulates one part of the system and all thermal-hydraulic quantities are determined for each cell at incremental time steps.

An equation set is established by applying the generalized conservation equations presented in the previous section to the finite difference cells. Figure IV-1 shows the control volumes and the placement of variables within those cells. It should be noted that a standard staggered cell approach is used where the momentum equation is written for momentum cells and the continuity equation is written for continuity cells. The desire to use those definitions stems from requirements of the solution algorithm.

The finite difference equations for the mass conservation equations presented in Section III are written as follows:

Gaseous Air

$$(\alpha\rho_g - \alpha\rho_g^n)_j \, V_c / \Delta t + Fg_j - Fg_{j-1} = Sg \qquad (4.1)$$

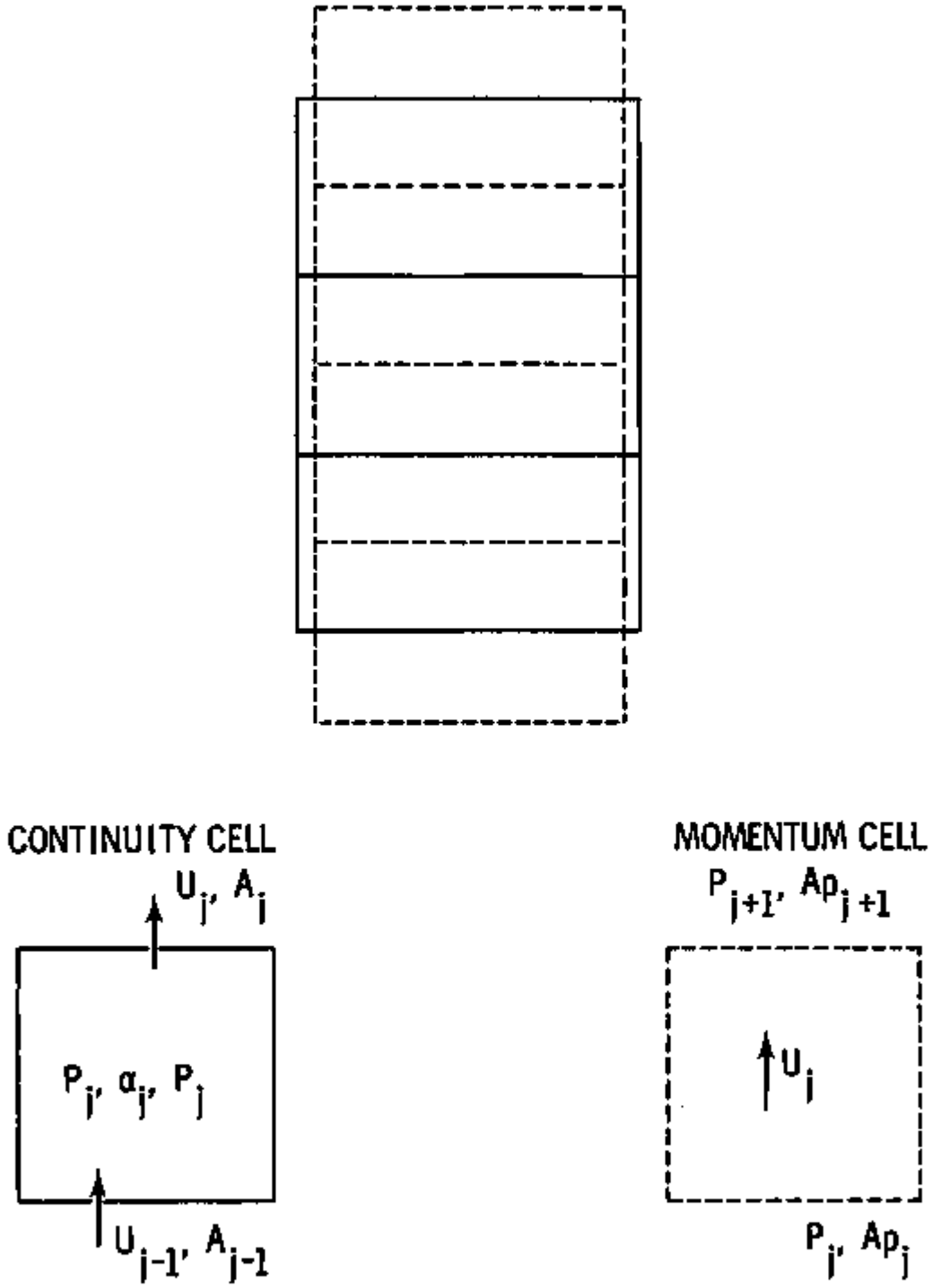


Figure IV-1. Calculational Cells.

where

$$F_{gj} = (\alpha^{*n}\rho_g^{*n}U_g A)_j \tag{4.2}$$

Water

$$\{ (1-\alpha)\rho_\ell - (1-\alpha)\rho_\ell^{\,n}\}_j V_c /\Delta t + F_{\ell j} - F_{\ell j-1} = 0 \tag{4.3}$$

where

$$F_{\ell j} = [ (1-\alpha)^{*n}\rho_\ell^{*n}U_\ell A]_j \tag{4.4}$$

Dissolved Air

$$\frac{[(1-\alpha)\rho a - (1-\alpha)^n \rho a^n]_j}{\Delta t} V_c + Fa_j - Fa_{j-1} = - S_{gj} \tag{4.5}$$

where

$$Fa_j = [ (1-\alpha)^{*n}\rho_a^{*n} U_\ell A]_j \tag{4.6}$$

The continuity cell volume is denoted by $V_c$, All quantities are understood to be at new time (n + 1) except those denoted by the old time (n). The superscript * denotes a central cell value assigned at a cell boundary. Donor assignment is determined by the velocity where, for example,

$$\alpha^{*n} = \begin{cases} \alpha_j^n & ; \quad U_g \geq 0 \\ \alpha_{j+1}^n & ; \quad U_g < 0 \end{cases}$$

This is a standard assignment used in computational fluid mechanics and is necessary for numerical stability.

The momentum equations presented in Section III are written as follows:

Gaseous Air

$$(F_g - F_g^n)_j \, V_m / (A\Delta t) + Fg_j^n \, (\Delta U_g)^* = \overline{\alpha A_p}^n \, (P_j - P_{j+1})$$
$$+ g \, (\alpha\rho)_g^n \, V_m - K_i V_m U_r - V_m K_{g\omega} \, (\alpha\rho)_g^n \, |U_g| \, U_g \qquad (4.7)$$
$$+ S_g^n \, (U_\ell - U_g)$$

Water and Dissolved Air

$$(F_\ell - F_\ell^n) \; V_m/(A\Delta t) + F_{\ell j}^n \, (\Delta U_\ell)^* = \overline{(1-\alpha) \, A_p}^n \, (P_j - P_{j+1})$$
$$+ g \, \overline{(1-\alpha)\rho_\ell}^n \; V_m + K_i V_m U_r - K_{\ell\omega} \, V_m \, (1-\alpha)^n \rho_\ell \, |U_\ell| \, U_\ell \qquad (4.8)$$

The momentum flux terms are evaluated at old time (n) and use donor cell assignment

$$(\Delta U)^* = \left\{ \begin{array}{ll} U_j - U_{j-1} & ; \; F_j \geq 0 \\ U_{j+1} - U_j & ; \; F_j < 0 \end{array} \right\} \qquad (4.9)$$

The momentum cell volume is given by $V_m$. The other averages are defined, for example, as

$$\overline{\alpha A_p} = \tfrac{1}{2} \, \{ \, (\alpha A_p)_j + (\alpha A_p)_{j+1} \, \} \qquad (4.10)$$

and

$$\overline{\alpha\rho_g} = [ (\alpha\rho_g)_j V_m^- + (\alpha\rho)_{j+1} V_m^+ ] / V_{mj} \qquad 4.10$$

where $V_m^+$ and $V_m^-$ are the volumes of the j+1 and j continuity volumes, respectively, residing in the j momentum cell. The numerical method selected to solve this equation set is similar to the ICE[3] algorithm developed at the Los Alamos Scientific Laboratory. The method is iterative and implicit except for those terms indicated at old time (n). Due to the inclusion of the explicit terms, time step size is limited by a Courant condition. This limits time steps to be less than the fluid transit time through a computational cell.

The solution consists of two principal parts. The first is to solve for tentative new time flows from the momentum equations using presently known values for pressure, density and void fraction. These new flows satisfy the momentum equations but, in general, they do not satisfy the mass conservation equations. The second part of the solution is an iterative procedure where the flows, pressures, densities, dissolved air concentration, and void fractions are updated such that the momentum equations remain satisfied and the residual error in the mass conservation equations is reduced. The iteration procedure continues until the maximum mass conservation error in any finite difference cell is less than a selected value.

The iterative part of the solution is based on the volumetric form of the mixture mass conservation equation written as a function of known quantities and new time pressure; all dependent variables having been replaced by relationships which are themselves functions of only known quantities and new time pressures.

Completing this rearrangement changes the problem from one of many unknowns and many equations to one equation, the volumetric mixture mass conservation equation, and one unknown, pressure. The resulting equation is nonlinear in pressure and therefore requires iteration for solution, but the overall solution is more easily accomplished, and therefore is relatively economical, with respect to alternatives.

Details of the solution are presented in the following order having the indicated objectives:

1. Statement of the volumetric mass conservation equation to detail which variables must be replaced as functions of pressure;
2. Obtain the appropriate functional relationships of variables indicated in (1) to enable the composition of the desired pressure equation; and,
3. Provide details of the pressure solution and back substitution used to evaluate dependent variables.

Volumetric Continuity Equation

The volumetric mixture mass conservation equation is a key to the solution method in that all variables within it will be replaced by functions of known quantities and new time pressure. The first step in the derivation requires expanding the temporal terms of Equations (4.1) and (4.2) and dividing each by $\rho_k V_c$ to obtain:

for the liquid,

$$[\ (1-\alpha) - (1-\alpha)^n\ ]/\Delta t\ + [\ F_{\ell j} - F_{\ell j-1}\ ]\ /\ (\rho_{\ell j}\ V_c) \approx 0 \tag{4.11}$$

and for the vapor,

$$[\ \alpha - \alpha^n\ ]/\Delta t\ +\ \alpha^n\ [\ \rho_g - \rho_g^n\ ]/(\rho_g \Delta t) +\ [\ F_{gj} - F_{gj-1}\ ]/ \tag{4.12}$$

$$(\rho_g V_c) \approx S_g/(\rho_g V_c)$$

where it has been assumed that the liquid density is constant. The volumetric mixture mass conservation equation is the result of adding Equations (4.11) and (4.12)

$$\alpha^n\ [\ \rho_g - \rho_g^n\ ]/(\rho_g \Delta t) + [\ F_{\ell j} - F_{\ell j-1}\ ]/(\rho_\ell V_c) + [\ F_{gj} - F_{gj-1}\ ]/(\rho_g V_c) \tag{4.13}$$

$$- S_g/(\rho_g V_c) = 0$$

It is evident from Equation (4.13) that to obtain the desired pressure equation, $\rho_g$, $F_v$, $F_l$ and $S_g$ must be stated as functions of pressure. Pressure relationships for $F_l$ and $F_v$ are obtained from the momentum equations, that for $\rho_g$ is available from the equation of state, and for the air source, $S_g = K(1-\alpha)^n (\rho_a - \rho_{asat})$, it is obtained from the equation of state for $\rho_{asat}$ and the continuity equation for $\rho_a$. Specifics of the required equation manipulations follow.

## $F_l$ and $F_v$ as Functions of Pressure

The momentum equations must be rearranged and solved simultaneously to obtain the liquid and vapor flow rates as a function of pressure because the interfacial shear, contains contributions from both the liquid and the vapor.

Old time quantities are first combined and defined as follows:

$$L^n = F_\ell^n + A\Delta t/V_m \left[ V_m \overline{\alpha_\ell \rho_\ell}^n g - F_\ell^n \Delta U_\ell^* \right] \tag{4.14}$$

$$V^n = F_g^n + A\Delta t/V_m \left[ V_m \overline{\alpha \rho}_g^n g - F_g^n \Delta U_g^* \right] \tag{4.15}$$

Equations (4.6) and (4.7) are then rearranged to obtain

$$F_\ell * RKL = L^n + A\Delta t/V_m \left[ g_c (P_j - P_{j+1}) \overline{(1-\alpha)A_p}^n + V_m K_i C_{ov}/(\alpha^n \rho_g^n A) F_g \right] \tag{4.16}$$

$$F_g * RKV = V^n + A\Delta t/V_m \left[ g_c (P_j - P_{j+1}) \overline{\alpha A_p}^n + (S_g^n + K_i V_m C_{o\ell})/( (1-\alpha)^n \rho_\ell^n A) F_\ell \right] \tag{4.17}$$

where

$$RKL = 1 + \Delta t/\left( (1-\alpha)^{n} \rho_{\ell}^{n} \right) \left[ Co_{\ell} K_i + K_{\ell w} (1-\alpha)\rho_{\ell} |U_{\ell}| \right]^{n} \qquad (4.18)$$

$$RKV = 1 + \Delta t/(\alpha^{n} \rho_{g}^{n}) \left[ C_{ov} K_i + K_{gw} \alpha \rho_{g} |U_{g}| + S_{g}/V_{m} \right]^{n} \qquad (4.19)$$

Equations (4.16) and (4.17) are then combined to solve for $F_g$ and $F_l$. The results are shown below

$$F_g = \{ V^{n} + A\Delta t/V_{m} \left[ g_c (P_j - P_{j+1}) \overline{(\alpha A p}^{n} + \right. \qquad (4.20)$$

$$\left. \overline{(1-\alpha)A_p}^{n} \Delta t \left( S_{g}^{n}/V_{m} + K_i C_{o\ell} \right)/\left[ (1-\alpha)^{n} \rho_{\ell}^{n} RKL \right) \right] \right]$$

$$+ L^{n} \Delta t/\left( (1-\alpha)^{n} \rho_{\ell}^{n} RKL \right) \left( S_{g}^{n}/V_{m} + K_i C_{o\ell} \right) \}$$

$$/ \{ RKV - \Delta t^{2} K_i/\left( (1-\alpha)^{n} \rho_{\ell}^{n} \alpha^{n} \rho_{g}^{n} \right) \left( S_{g}^{n}/V_{m} + K_i C_{o\ell} \right) \}$$

$$F_{\ell} = \{ L^{n} + A\Delta t/V_{m} \left[ g_c (P_j - P_{j+1}) \left( \overline{(1-\alpha)A_p}^{n} \right. \right. \qquad (4.21)$$

$$\left. \left. + \Delta t K_i C_{ov} \overline{\alpha A}_{p}^{n}/(\alpha^{n} \rho_{g}^{n} RKV) \right) \right] + \Delta t K_i C_{ov}/(\alpha^{n} \rho_{g}^{n} RKV) V^{n} \} /$$

$$\{ RKL - \Delta t^{2} K_i C_{ov}/(\alpha^{n} \rho_{g}^{n} RKV (1-\alpha)^{n} \rho_{\ell}^{n}) (S_{g}^{n}/V_{m} + K_i) \}$$

Coefficients are defined to reduce the momentum equations to a more tractable form; definitions of the coefficients follow immediately from Equations (4.20) and (4.21) above.

$$F_g = M_g^n + M_{pg}^n (P_j - P_{j+1}) \tag{4.22}$$

$$F_\ell = M_\ell^n + M_{p\ell}^n (P_j - P_{j+1}) \tag{4.23}$$

Equations (4.22) and (4.23) have the desired form that the liquid and vapor flows are dependent on coefficients determined from old time quantities and on the new time pressures.

## $\rho_g$ as a Function of Pressure

The pressure relationship for $\rho_g$ is available through the equation of state, $P = \rho_g RT$. Because the system is assumed to operate isothermally,

$$\frac{\partial \rho_g}{\partial t} = \frac{\partial \rho_g}{\partial P} \frac{\partial P}{\partial t} = \frac{1}{RT} \frac{\partial P}{\partial t} \tag{4.24}$$

## $S_g$ as a Function of Pressure

The pressure dependence of the air source, $S_g = K_g V_c (1-\alpha)^n (\rho_a - \rho_{asat})$, is obtained by solving for $\rho_a$ and $\rho_{asat}$ as a function of pressure and substituting those relationships into the definition. Equation (3.13), the equation of state for $\rho_{asat}$ may be used directly. The pressure dependence of $\rho_a$ is obtained as follows.

The liquid continuity equation is first multiplied by $\rho_{aj} / \rho_l$ and subtracted from the dissolved air continuity equation to yield,

$$\begin{aligned} &(1-\alpha)^n V_c (\rho_a^n - \rho_a) / \Delta t + (\rho_a^{*n} - \rho_{aj}) F_{\ell j}/\rho_\ell \\ &- (\rho_{aj-1}^{*n} - \rho_{aj}) F_{\ell j-1} / \rho_\ell = - k_g V_c (1-\alpha)^n (\rho_a - \rho_{asat}) \end{aligned} \tag{4.25}$$

Equation (4.25) is then solved for $\rho_a$.

$$\rho_a = [\ (1-\alpha)^n \rho_a^n V_c/\Delta t - \rho_a^{*n} F_{\ell j}/\rho_\ell + \rho_a^{*n} F_{\ell j-1}/\rho_\ell + K_g V_c\ (1-\alpha)^n \rho_{asat}\ ]/$$
$$[\ (1-\alpha)^n V_c/\Delta t - F_{\ell j}/\rho_\ell + F_{\ell j-1}/\rho_\ell + K_g V_c (1-\alpha)^n\ ] \qquad (4.26)$$

Substitution of the liquid momentum equation for $F_l$ and of the equation of state for $\rho_{asat}$ produces the desired functional form, $\rho_a = f(p)$.

The Pressure Equation

Substituting the preceeding relationships for $\rho_g$, $F_v$ $F_l$ and $S_g$ into the volumetric form of the mixture mass conservation equation (Equation (4.13)) yields an equation which is a function of only old time qualities and new time pressure. The result is called the pressure equation, and is solved iteratively by a Newton-Raphson method. The solution method is described next.

Solution of the Pressure Equation

The solution sequence begins by evaluating tentative values for the liquid and vapor flows, $F_l$ and $F_v$, via the momentum relationships, Equations (4.22) and (4.23), based on old time pressures.

The mixture mass conservation equation will not necessarily be satisfied by these flows and an error will therefore exist. In functional form this can be expressed as

$$C(P) = E \qquad (4.27)$$

where C is the volumetric mixture mass conservation equation (Equation (4.13)) and E is the error. We now desire a pressure correction to reduce the error to zero. The specific pressure correction is obtained by differentiating Equation (4.27) with respect to pressure and rearranging to obtain

$$[\ \delta C(P)/\delta P_{j+1}\ ]\ \delta P_{j+1} + [\ \delta C(P)/\delta P_j\ ]\ \delta P_j + [\ \delta C(P)/\delta P_{j-1}\ ]\ \delta P_{j-1} = \delta E \qquad (4.28)$$

The required error correction is determined such that the current error plus the to-be-evaluated correction equals zero, ie, $E_j + \delta E = 0$, or $\delta E = -E_j$. With knowledge of the pressure dependence of the mixture mass conservation equation, it is laborious but straight forward to obtain the coefficients $\delta C/\delta P_j$, $\delta C/\delta P_{j-1}$, and $\delta C/\delta P_{j+1}$. The set of Equations (4.28) for all cells is a tridiagonal matrix which is solved very efficiently for $\delta P_j$. New pressures are then evaluated, $P = P + \delta P$. The liquid and vapor flow rates are updated via the momentum equations, $\rho_g$ and $\rho_{asat}$ are updated from the equations of state, $\rho_a$ is updated via Equation (4.26) and the air source is updated via Equation (3.17). The void fraction is also updated at this time by solving the combined gas/liquid continuity equation for $\alpha$, applying the constraint, $.0001 < \alpha < .9999$, so that a small amount of each phase is always present in each calculation cell.

If equation (4.27) was linear in pressure, the newly calculated tentative solution would exactly satisfy the momentum and continuity equations; however, it is nonlinear in pressure and the just described solution does not exactly satisfy the equation set. Iteration is thus required, and the procedure (evaluate the volumetric continuity error; update the pressure, flow rates, $\rho_{asat}$, $\rho_g$, $\rho_a$, $S_g$ and $\alpha$) must be repeated until the maximum error is less than a small, user-determined value.

## Section V

## CODE VERIFICATION

Comparisons between calculations and analytical solutions for a frictionless and damped CAES system have been performed to aid in code verification. These hypothetical test problems consider a closed cavern, U-bend and compensation leg. Three initial conditions: high water level, low water level and water level within the U-bend, cover the range of conditions for which this code was designed. A small perturbation is introduced at time 0.0 and the oscillatory fluid response is calculated and compared to the analytical solution.

These sample problems test the coding of vapor compressibility and the overal continuity-momentum equation solution. The air source has been set to zero and, therefore, these calculations do not offer verification for that process or any significant two-fluid interactions.

Figure V-1 illustrates the system and intial condition with the liquid level in the U-bend. Given a perturbation, the oscillation perid from the exact solution is 43.7 seconds. Figure V-2 shows the calculated response and the 43.7 second period from the exact solution. The results are in excellent agreement.

Figure V-3 shows the high water level initial condition and the exact solution period of 133.0 seconds. The difference between the high water level period and that when the water level was in the U-bend is due to the relative importance of compressibility and due to the significant area change between the cavern and the compensation leg. Results of the calculation and the exact solution are shown in Figure V-4. The agreement is again excellent.

Linear frictional damping, -Cu, was then added to this problem to obtain an underdamped flow response. The analytical solution for this problem yields a damped oscillation with period equal to that of the

FRICTIONLESS,

$$T = \frac{2\pi}{W} = \frac{2\pi}{\sqrt{2g/L}} = 43.7 \text{ SEC}$$

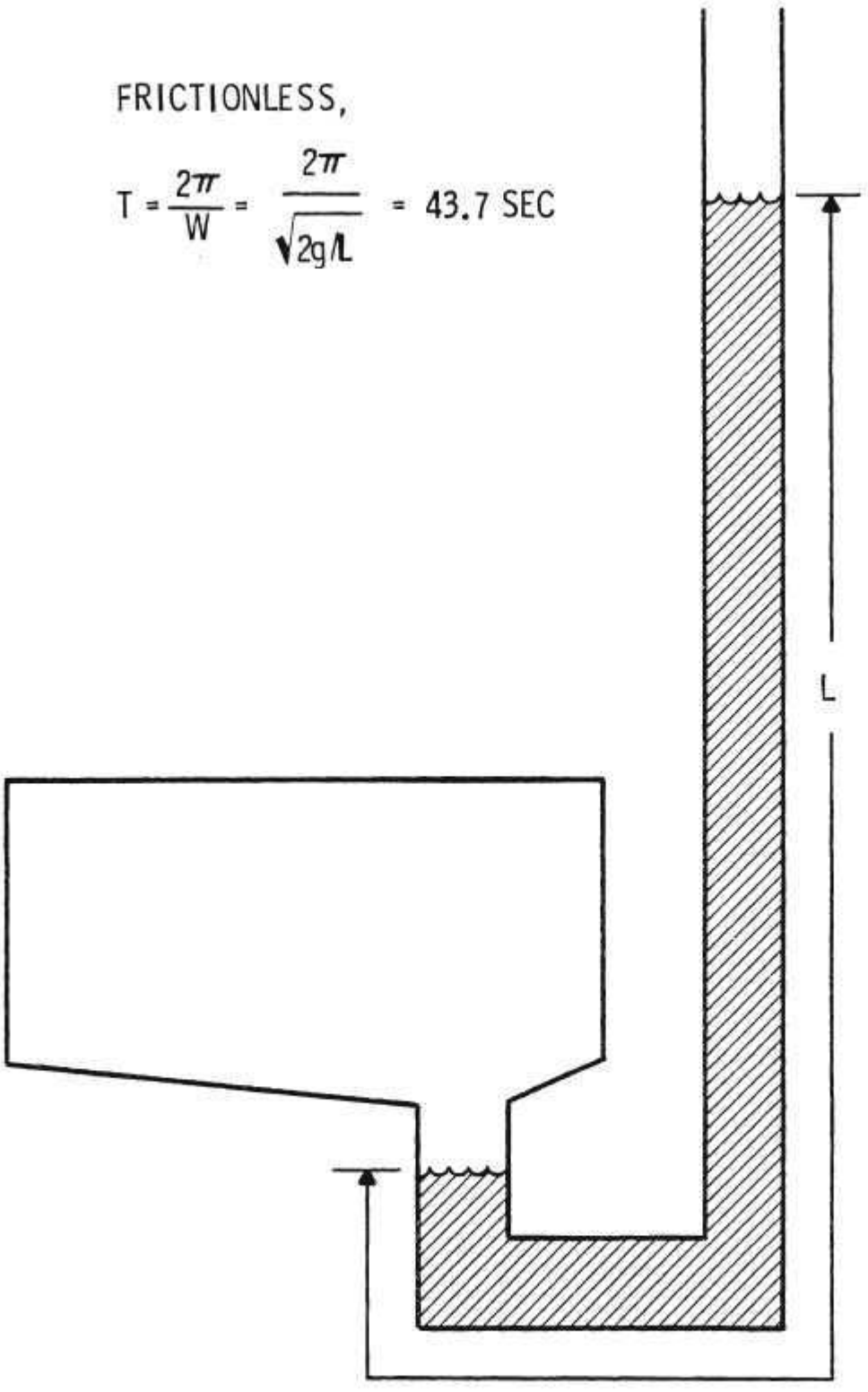


Figure V-1. Liquid Level In U-Bend.

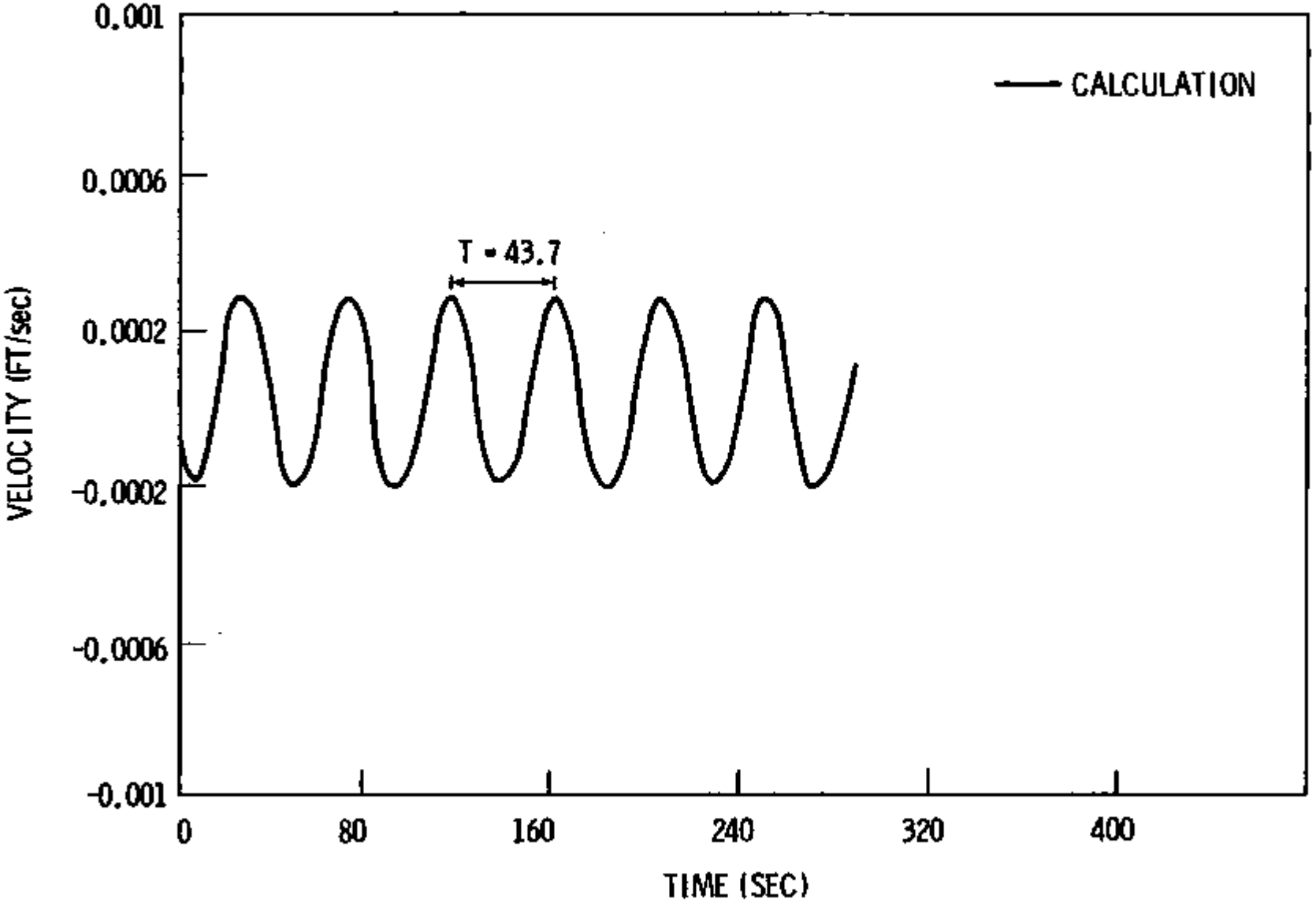


Figure V-2. Water Level In U-Bend, Frictionless.

FRICTIONLESS,

$$W = \sqrt{g\left[\frac{(H+2L_2)\,A_1}{L_1L_2\quad A_2}\right]}$$

$$T = \frac{2\pi}{W} = 133 \text{ sec}$$

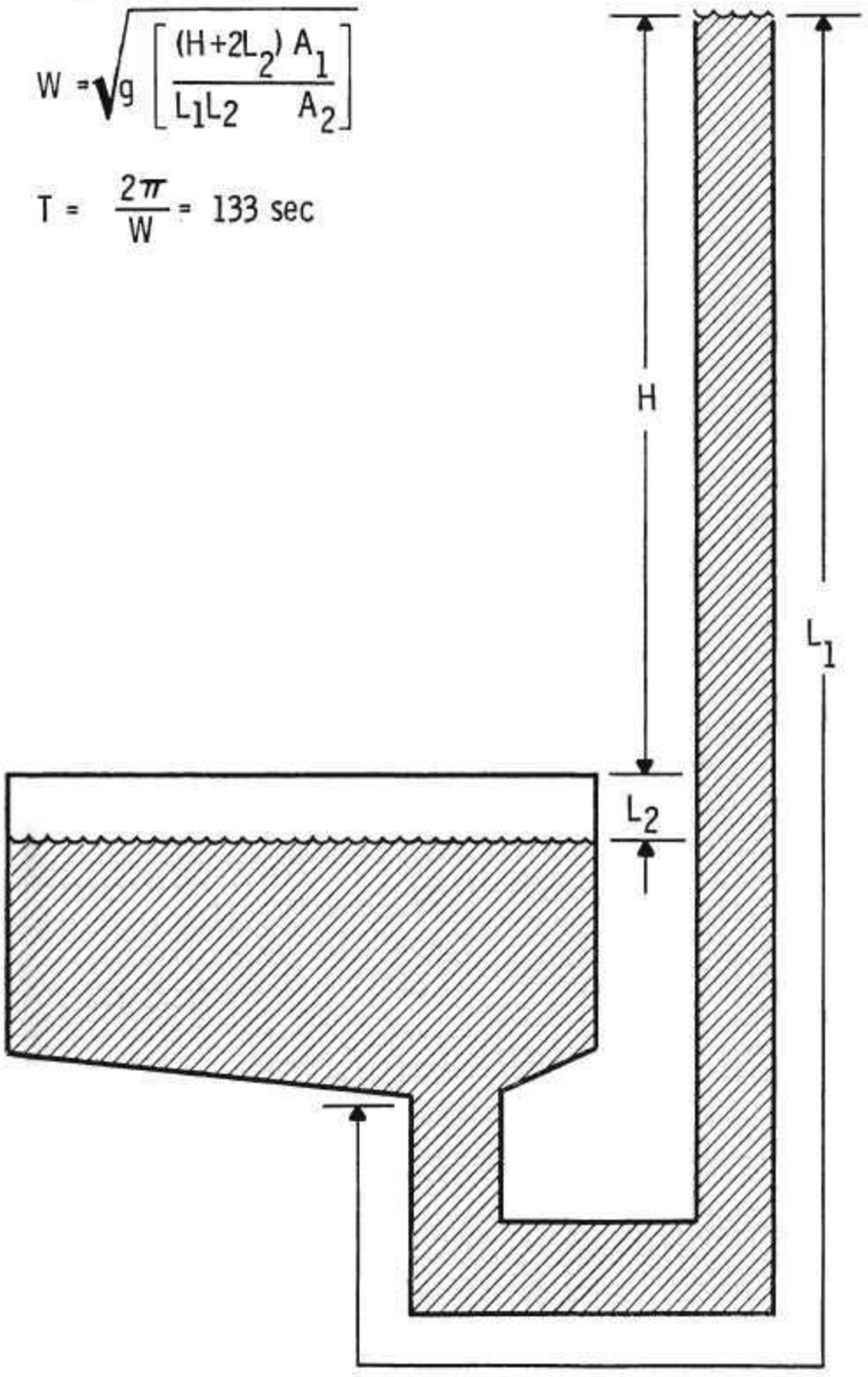


Figure V-3. Liquid Level At High Water Level Position.

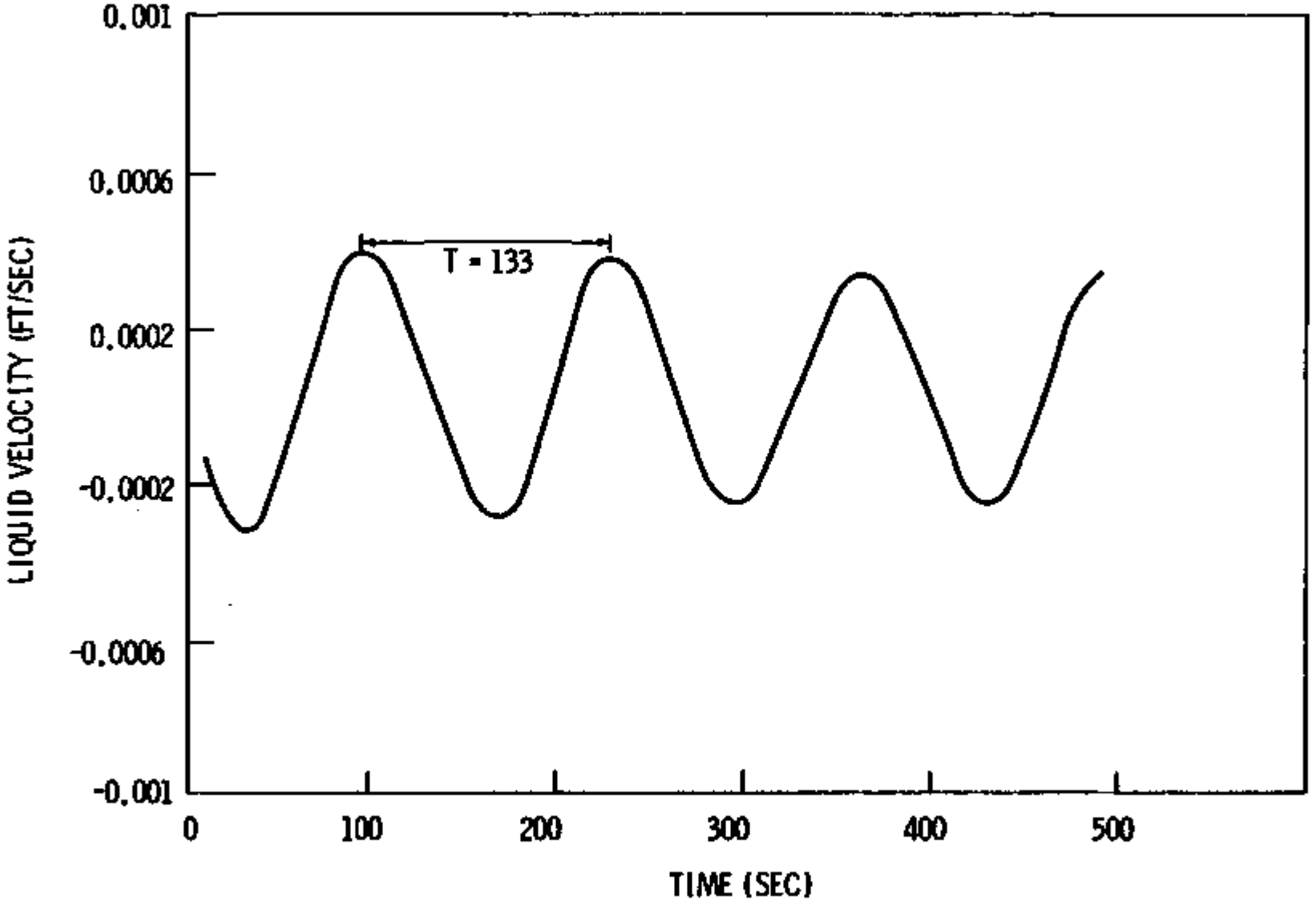


Figure V-4. High Water Level, Frictionless.

frictionless case and a 30% damping between oscillations, dictated by the selection of the friction coefficient, C. Figure V-5 shows that the calculation and exact solution are in good agreement.

The last test problem simulates the low water level condition depicted in Figure V-6. The period from the exact solution, 388.0 seconds is shown along with the calculated results in Figure V-7.

While these sample calculations are necessarily simplified representations of flow response in CAES, they do demonstrate that the dynamics of flow oscillations are correctly calculated by the computer program. Including more complex phenomena in these test problems, such as the release of dissolved air, would eliminate the possibility of comparing to a simple exact solution. Demonstration of the computer program's predictive ability for more complex situations therefore requires comparison to experimental data or other engineering estimates of the Champagne Effect.

It would be desirable to have detailed data pertaining to oscillatory two-phase flow with dissolved air releases at varying degrees of air saturation and pipe diameter. Experimental data including all phenomenal expected in CAES systems is unfortunately not known to be publically available, and it is therefore not possible to verify all models used in the computer program.

The present unavailability of certain experimental data does not, however, negate the usefullness of this analysis tool because many of the areas of uncertainty can be bounded by physical and observed limitations. The air source is one such example, and although a precise description of air release may never be possible, in the limit it is known that air release can be no greater than that defined by saturation.

This computer program has been designed with knowledge of these uncertainties, and it has consequently been structured to allow user investigation of a wide range of constitutive models and parameters.

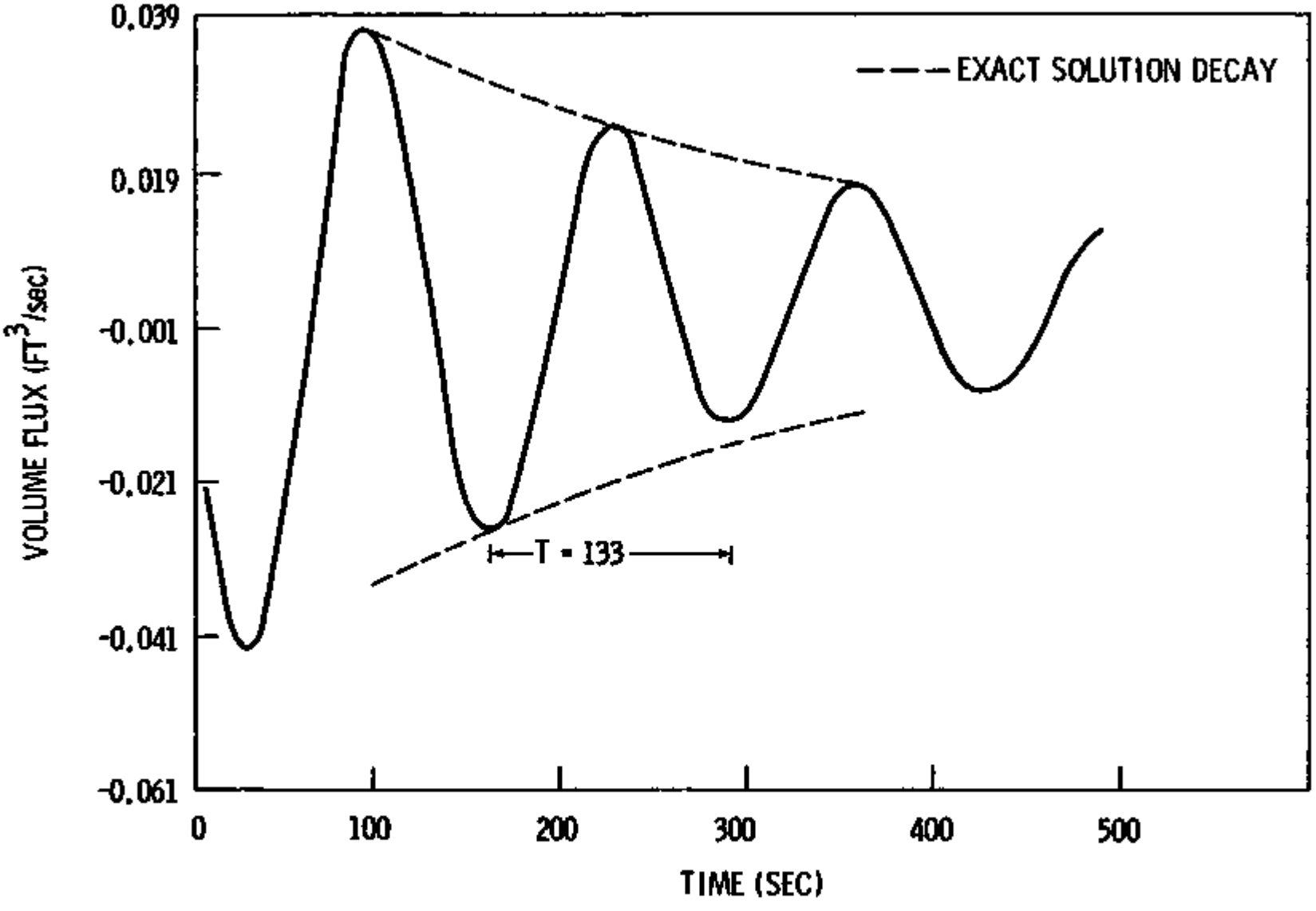


Figure V-5. High Water Level with Friction.

FRICTIONLESS,

$$W = \sqrt{g \left[ \frac{(H+2L_2)\ A_1}{L_1 L_2 \quad A_2} \right]}$$

$$T = \frac{2\pi}{W} = 388 \text{ SECONDS}$$

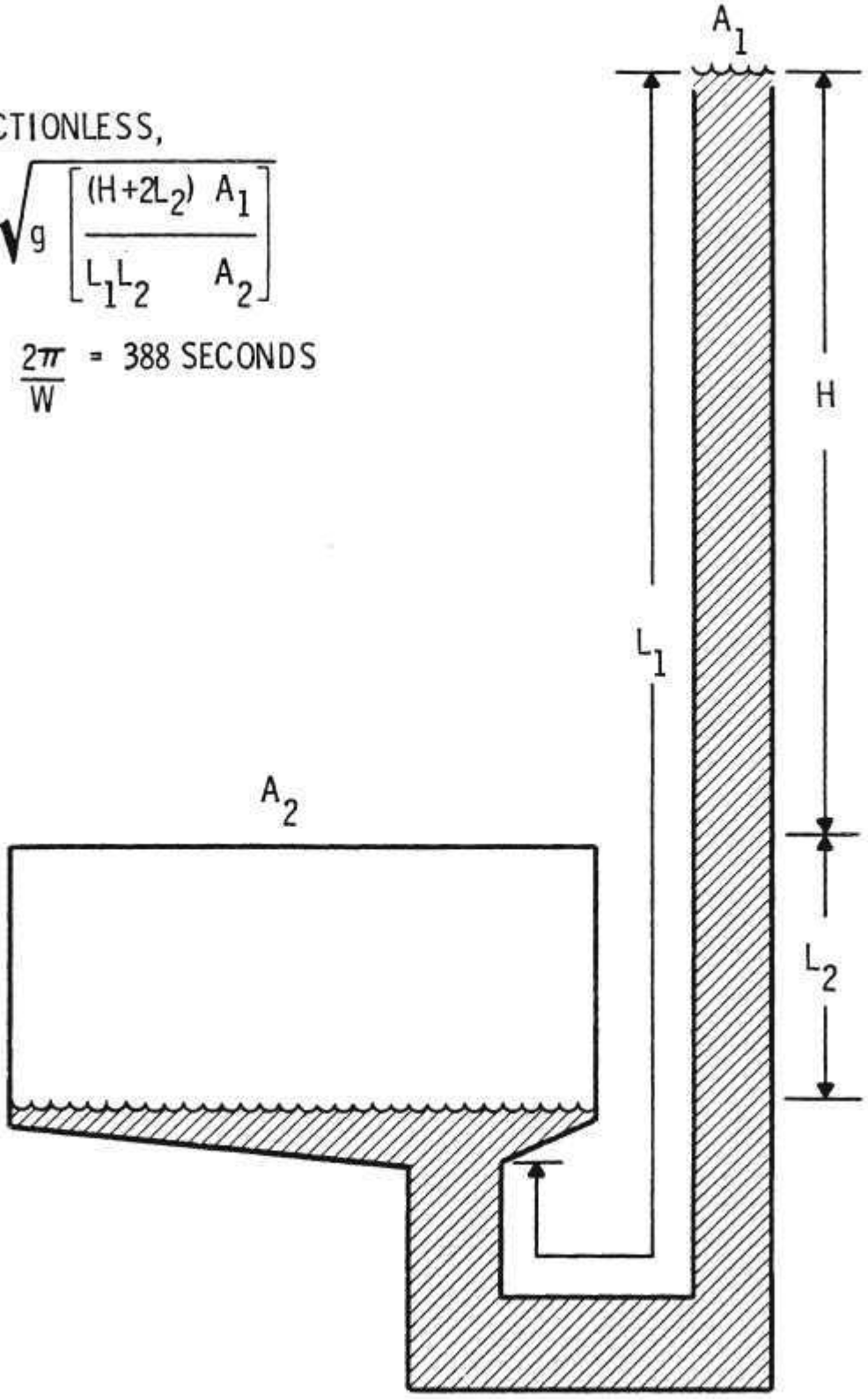


Figure V-6. Initial Condition.

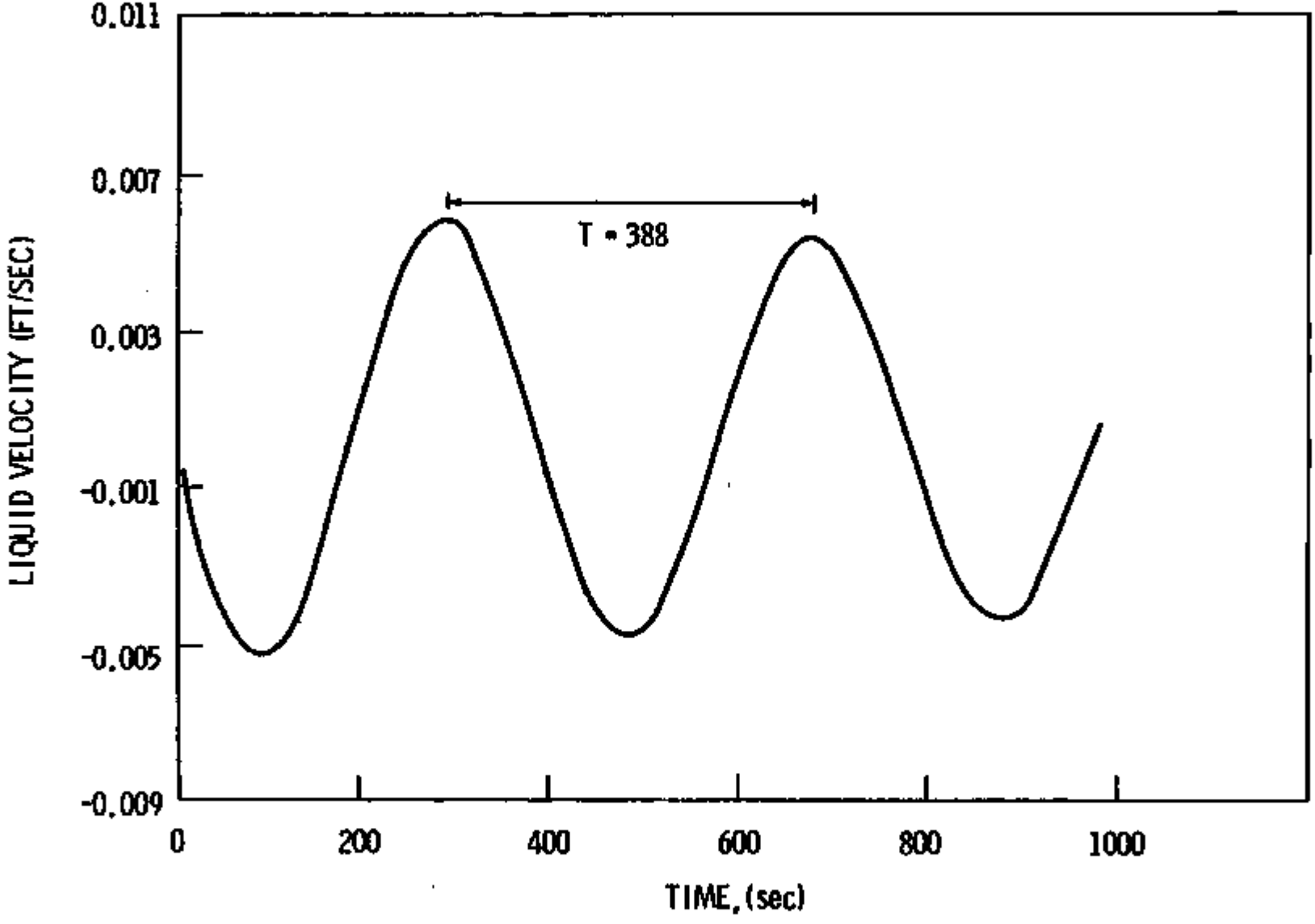


Figure V-7. Low Water Level, Frictionless

The significance of the recognized uncertainties is that they pertain to constitutive relationships and not the general analysis model which is thought to be general and descriptive of Champagne Effect phenomena.

## Section VI

## ANALYSIS RESULTS

The analytical model was used to calculate the dynamic response of a CAES facility similar to that proposed by Acres American for PEPCO. The purpose of these calculations was to provide enlightenment of the operational characteristics of the system with respect to the Champagne Effect. While no attempt was made to optimize the proposed design, it is hoped that these results can clarify current design issues and indicate directions for design refinement.

The analysis consisted of two parts. The first was a study of individual parameters to access specific impact on the Champagne Effect from design, operational and constitutive model features. This part was conducted as a comparative effect study. A base case was selected and compared to calculations where one specific change was made to ascertain if the system was more or less stable. This analysis provided a table of parameters that improve, aggrevate, or are neutral with respect to the influence of the Champagne Effect on operations.

It was then possible to proceed to the second part of the analysis--a "worst case" simulation. Given the design, parameters were selected to accentuate the influence of the Champagne Effect and thereby create a worst case type problem. It should be noted that no attempt was made to find the worst combination of parameters. Rather, within the context of a reasonable design and constitutive modeling bounded either by physical or experimentally determined limits, calculational inputs were established consistent with the findings from the separate effect comparisons that accentuated the Champagne Effect. Results of this calculation indicate that the Champagne Effect is unlikely to cause blowout for a properly designed CAES system.

## SEPARATE EFFECT STUDY

Results of the separate effect study are summarized in Table VI-1 showing design, operational and correlation parameters that reduce the influence of the Champagne Effect on CAES operation. Calculations to support this listing are not detailed; however, general comments follow on each point to impart the relative significance of each and to assure that each is understood.

### Design

#### Deep Surface Reservoir

A deep surface reservoir suppresses the Champagne Effect because the pressure at the bottom of the reservoir is relatively constant at the hydrostatic pressure for liquid. For example, a reservoir 100 feet deep establishes an approximately constant, 4 atmosphere pressure at the compensation pipe; essentially eliminating the degradation of the hydrostatic head (the concern of the Champagne Effect) in this region. Also, the deep reservoir limits the Champagne Effect influence below the deep surface reservoir by providing a higher minimum pressure so that bubbles expand relatively less.

#### Provide Bottom Contouring

The cavern pressurization characteristic changes dramatically as the cavern empties and water level enters the U-bend. The reason for this change could be used to establish a desired low water-level cavern pressure response. The basic idea is to contour the bottom of the cavern to provide additional water level change per unit of volume of air stored prior to the water level entering the U-bend.

The following sketch shows that the above idea might be implemented by providing a well in the cavern at the U-bend entrance.

- Design Parameters
  - Include deep surface reservoir
  - Provide cavern bottom contouring
  - Modify design (not yet considered)
    - U-bend
    - Flow restricting orifice
    - Pipe Diameter

- Operational Parameters
  - Reduce compressor start-up rate
  - Reduce compressor flow rate
  - Impede air dissolution rate
  - Charge from high water level

- Correlation Parameters
  - Increased Wall Friction
  - Reduced interfacial friction
  - Model nonequilibrium air source

Table VI-1. Parameter Variations Reducing the Champagne Effect.

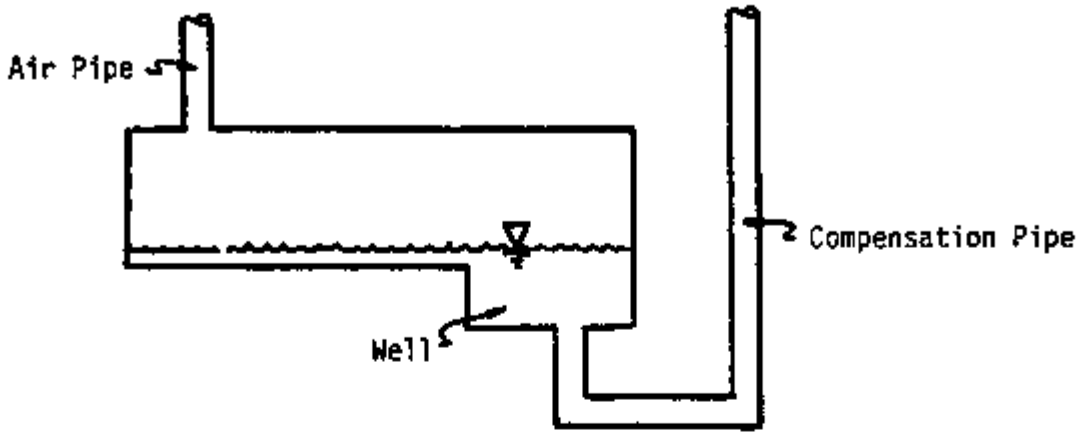


When the water level is above the cavern floor, the pressure in the cavern increases slightly as air is charged into the cavern. This is because the stored air volume expands against the nearly constant hydrostatic pressure. The hydrostatic pressure, however, increases slightly as cavern water level decreases assuming for now there is no head degradation from the Champagne Effect. When the water level enters the well, the stored air volume continues to expand; however, the hydrostatic pressure now builds at a faster rate per unit of air charged into the cavern. The net effect of this change is that the volume expansion of the cavern air is less and there is lower velocity flow in the compensation pipe.

The primary difference between the above idea and the hydrostatic head effect of the U-bend is one of dynamics and pressurization characteristic. If the cavern empties with a high velocity in the U-bend, the resulting hydrostatic head increase would also have to stop the flow to reach equilibrium. The flow "inertia" would require a certain amount of U-bend depth for this to occur. From this analysis to date, it is not known if this would exceed the depth required to prevent blowout for an equilibrium cavern over pressure. This bottom contouring design feature could be viewed as a safety design feature should a designed flow restriction fail during operation. It is offered for consideration to the cavern designers.

Fluid Friction

The analysis results indicate that fluid friction provides damping to flow oscillations. It is also the factor which prevents uncontrolled cavern flow that could lead to blowout. It, together with the reduction in cavern pressure, also provides the forces which balance the reduced hydrostatic head caused by the Champagne Effect. The combination of these factors (cavern pressure, friction, reduced hydrostatic head) combine to define the steady operating point for the cavern once the start-up transient is completed.

The following sketch illustrates the effect of air saturation on the cavern pressure versus charging rate.

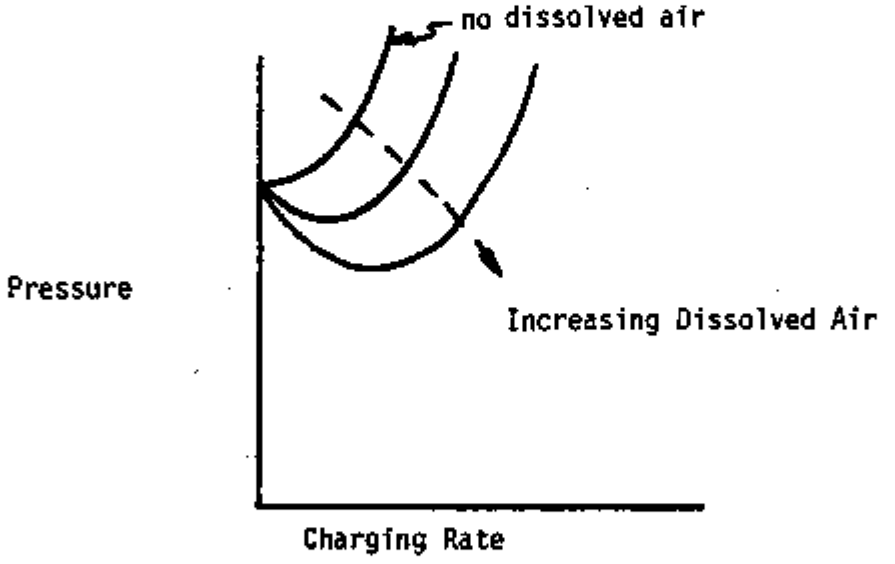


The cavern pressure is shown to increase with charging rate if the water does not contain dissolved air. This is caused by fluid friction. With increasing dissolved air, the pressure initially decreases with charging rate due to the reduction of hydrostatic head caused by the Champagne Effect. The pressure decrease stops as the charging rate increases due to increased frictional resistance from the higher flow rate. The amount of pressure reduction is related to the initial dissolved air concentration and the charging flow rate.

The following sketch illustrates the same plot for fixed initial dissolved air concentration, but as a function of the friction coefficient.

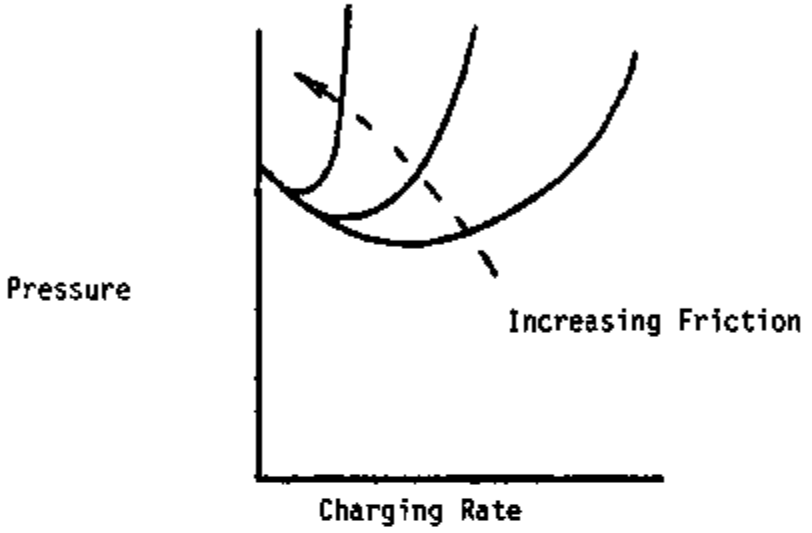


In both cases, friction turns the pressure curve around. The final operating point would depend upon operation and design specifics. Pipe diameter, surface roughness and placement of flow restrictions would be the primary options for the designer.

## Operational Parameters

### Reduce Compressor Start-up Rate

Compressor start-up rate is the time between the start of one compressor and the start of the next. Increasing this time allows the system more time to approach equilibrium with respect to previous compressor perturbations; thereby minimizing the impact of subsequent compressor flows.

### Reduce Compressor Flow Rate

The compressor flow rate effectively defines the magnitude of the start-up transient. Reduced compressor flow rates therefore lead to reduced flow and pressure oscillations.

### Impede Air Dissolution Rate

The initial amount of dissolved air in the liquid significantly affects the start-up transient because it is this amount of air that is available to cause the Champagne Effect. If actions are taken to impede the air dissolution rate, start-up transients will accordingly be reduced.

### Charge from High Water Level

All other parameters being the same, flow oscillations are maximum when start-up begins at the low water level. It may therefore be desirable, for example, to institute different charging schemes depending on water level position.

## Correlation Parameters

### Increased Wall Friction

Friction reduces the Champagne Effect by inhibiting the flow at any charging rate as was previously discussed. Surface roughness, pipe diameter and flow restrictions should therefore be designed accordingly. Friction factor correlations used in analysis should be selected carefully because of the significance of frictional forces.

### Reduced Interfacial Friction

Reducing interfacial friction either by a change in the bubble drag coefficient, $C_b$, or by increasing the distributional parameter, $C_0$, allows more gas to exit the compensation pipe and therefore reduces the Champagne Effect. Conservative coefficients are recommended when uncertainty exists.

### Nonequilibrium Air Source

Maximum flow oscillations in the calculations performed occur when the air source is modeled such that the maximum amount of air is released from the liquid. Reducing the transfer coefficient for nucleation or instituting a threshold supersaturation results in reduced oscillations.

## SAMPLE CALCULATIONS

It is desirable to have conservatively oriented calculations to assess the impact of the Champagne Effect on CAES operations because uncertainty exists in some parameters. Conservatism is obtained by bounding model input and not by changing the analytical model. The analytical model is quite general and dictates the phenomena that can be modeled; for example, inertial effects and relative phase motion are determined directly from the model. Conservatism is not obtained by altering this mathematical representation.

In an attempt to be conservative for these sample calculations, the model inputs were selected to accentuate the Champagne Effect.

Two sample calculations will be presented. Parameters adding to conservatism in the first calculation, a worst case simulation, are: 1) a low water level, 2) full charging rate, 3) maximum initial dissolved air, 4) approximately homogeneous wall friction, 5) interfacial friction for small diameter bubbles, and 6) equilibrium deaeration without dissolution. While we believe these specifications make the calculation highly conservative, we did not attempt to find "the" worst case.

The boundary conditions for this case are atmospheric pressure at the reservoir and a sequential start-up of the four compressors at five minute intervals with a 15 second start-up ramp between initiation and full flow for each compressor. A maximum air flow of 2640 lbm/sec is obtained at 915 seconds and is maintained at that value for the remainder of the calculation. The nodalization and initial water level position is shown in Figure VI-1.

Figure VI-2 shows the volumetric flow rate of the charging air. The charging air initially pressurizes the cavern which in turn causes liquid to flow up the compensation pipe. Deaeration begins as the liquid motion causes local supersaturated of dissolved air. Degradation of the

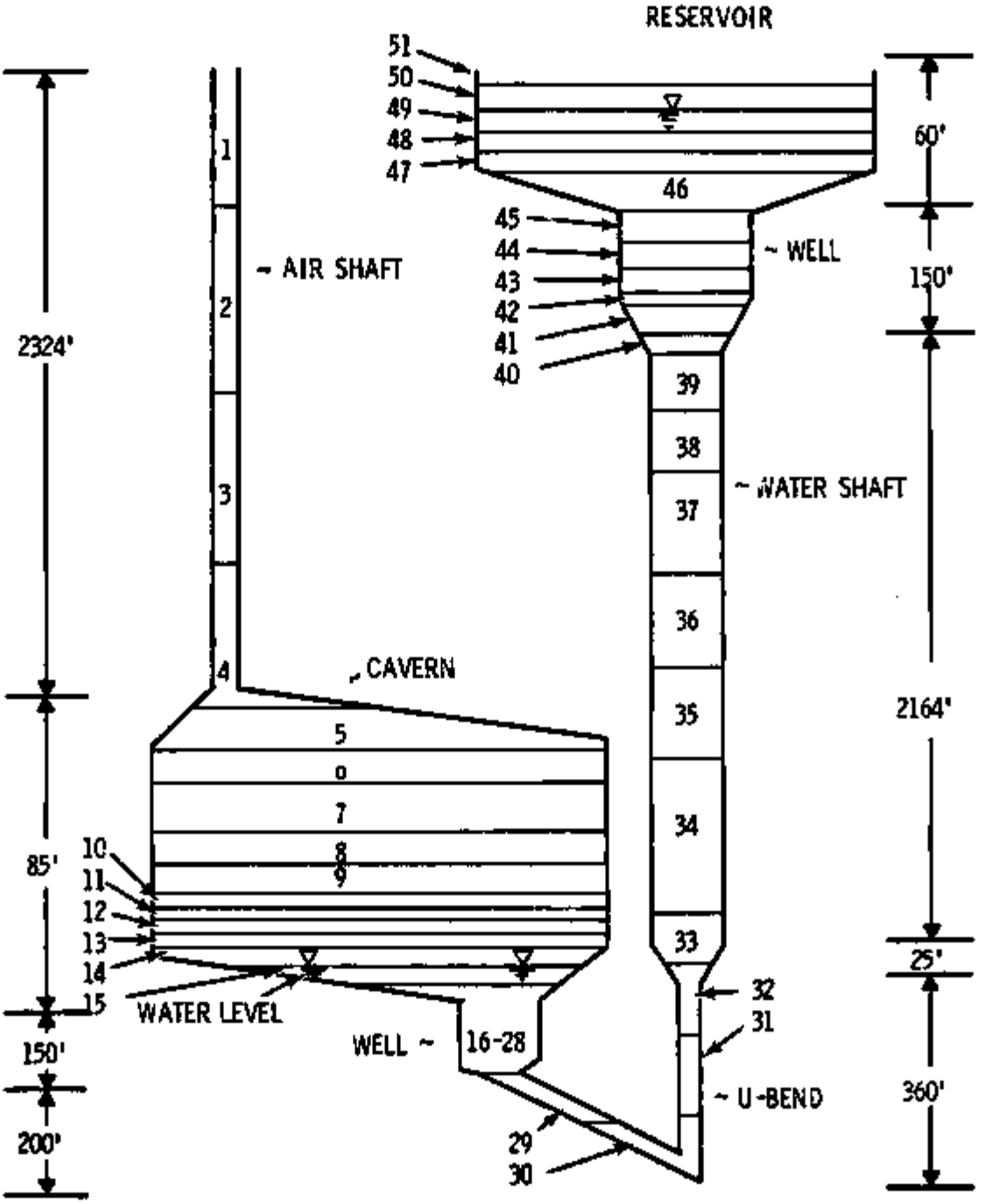


Figure VI-1. System Nodalization.

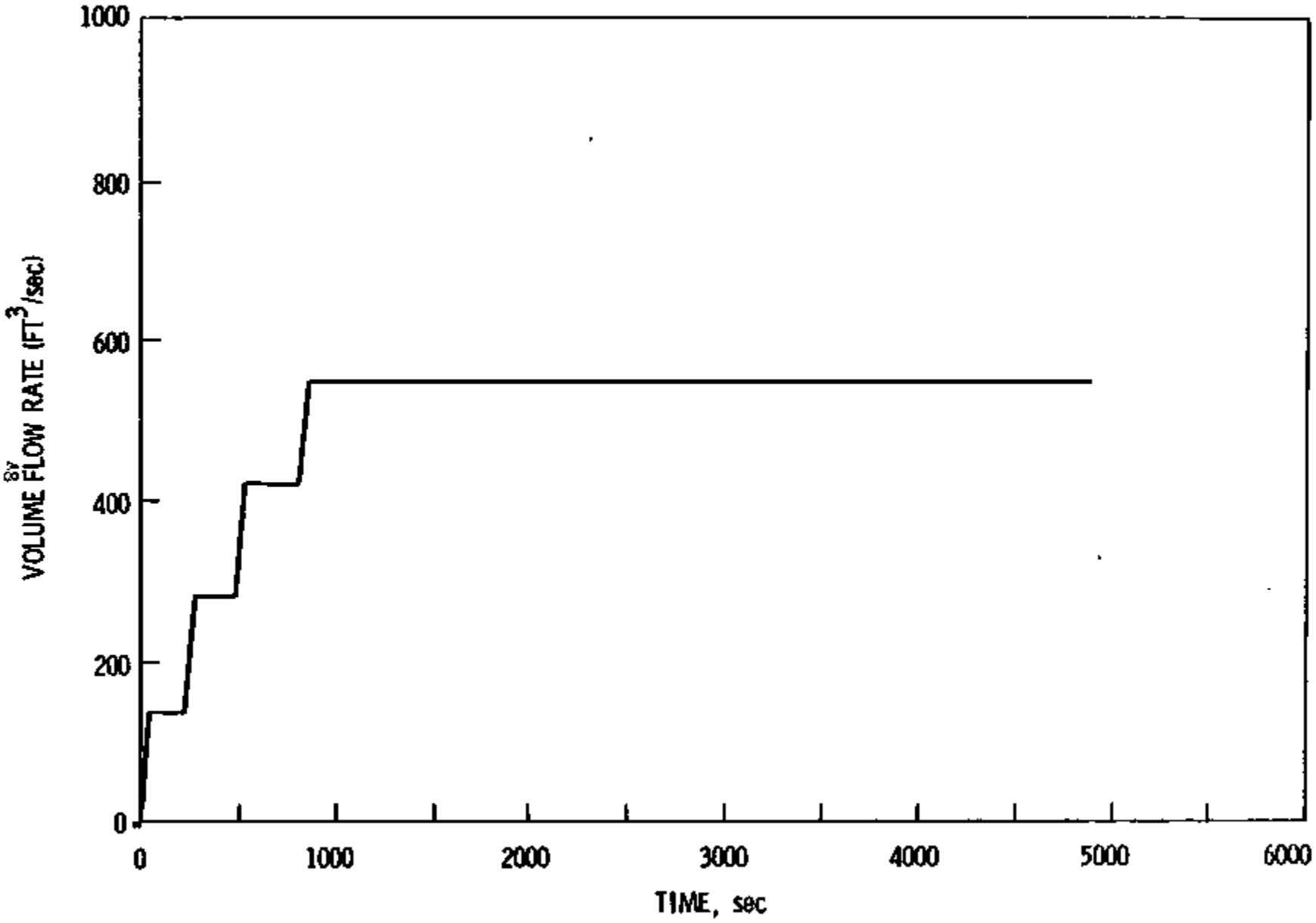


Figure VI-2. Inlet Volumetric Flow Rate of Air.

hydrostatic head results and fluid within the compensation pipe then accelerates toward the reservoir. Oscillations result in response to the forces previously discussed.

Figure VI-3 shows the liquid velocity at Node 39, the highest velocity region in the system. An oscillatory characteristic is shown with a maximum velocity of approximately 18 feet/second. The velocity is significantly reduced beyond 4000 seconds because the liquid level in the cavern has entered the well and the cavern begins pressurizing as the liquid level drops and the hydrostatic head correspondingly increases. This hydrostatic pressurization is a most important damping feature of CAES design. Figure VI-4 shows the air source at Node 39. The air source is positive during upflow as water containing a high concentration of dissolved air enters this region. During flow reversal, the air source is zero because liquid with a low air concentration from the reservoir flows into the higher pressure compensation pipe. The flow reversal also causes a reduction in the dissolved air concentration throughout the compensation pipe. Figure VI-5 shows the cavern pressure at Node 6. Pressure decreases are consistent with the air release and associated pres-reduction in hydrostatic head in the compensation pipe. The pressure increase starting at approximately 4000 seconds is caused by an increasing hydrostatic head as the liquid level drops from the large area cavern to the relatively small area well. Figure VI-6 shows the void fraction at Node 39. Maximum void fractions are consistent with periods of significant deaeration, minimum cavern pressure and maximum fluid velocity.

As a contrast to the full charging illustration at low water level, another calculation was run utilizing all features of the previous example except the initial cavern water level was raised to Node 6 of Figure VI-1. This case represents a more typical condition from which full charging would be applied. This calculation is also conservative with respect to the Champagne Effect because bounding initial conditions and constitutive relationships were again used. Figure VI-7 shows the resulting liquid and air velocities at Node 39. This result shows only modest oscillatory behavior and a quasi-steady condition is reached by 2000 seconds.

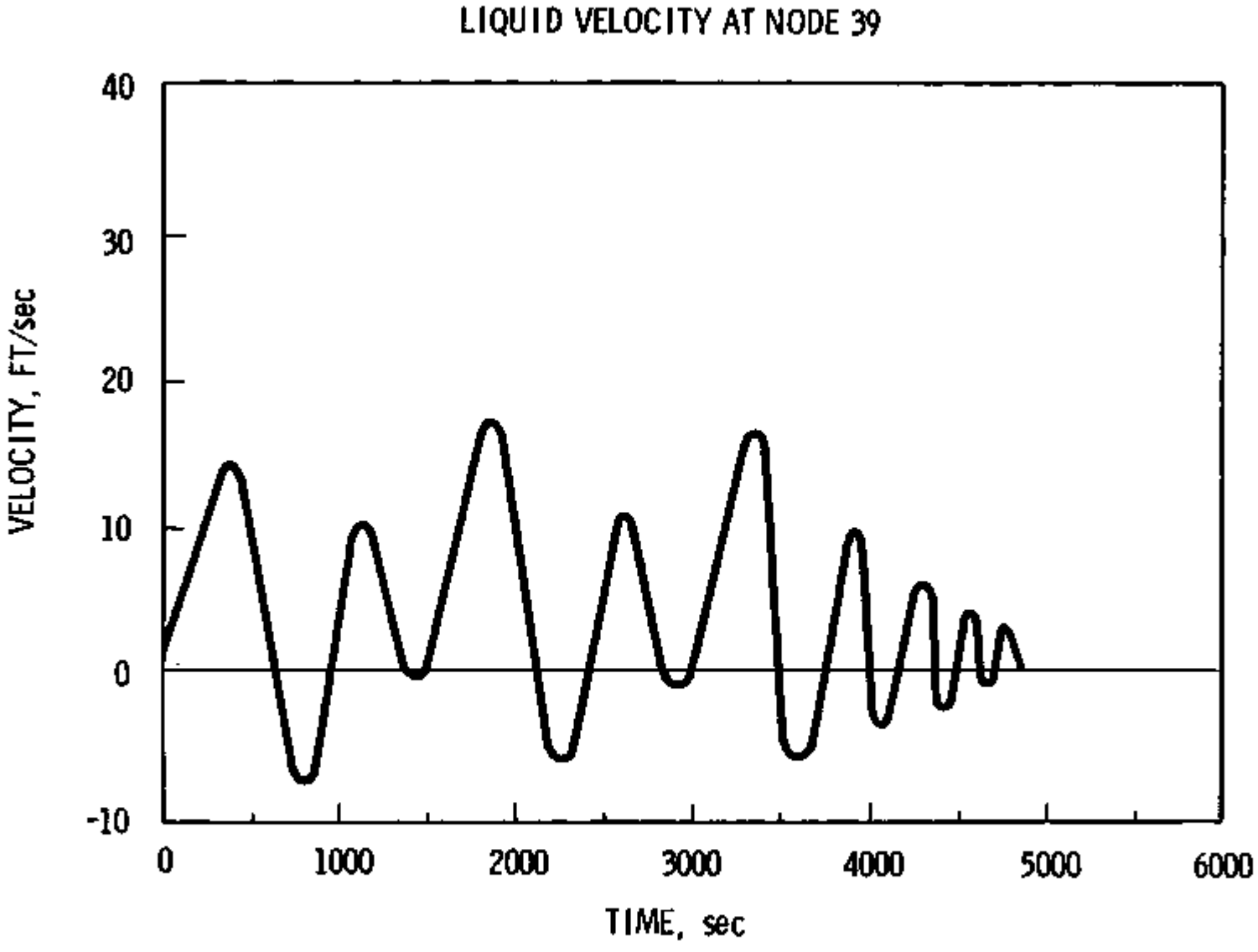


Figure VI-3. Liquid Velocity at Node 39.

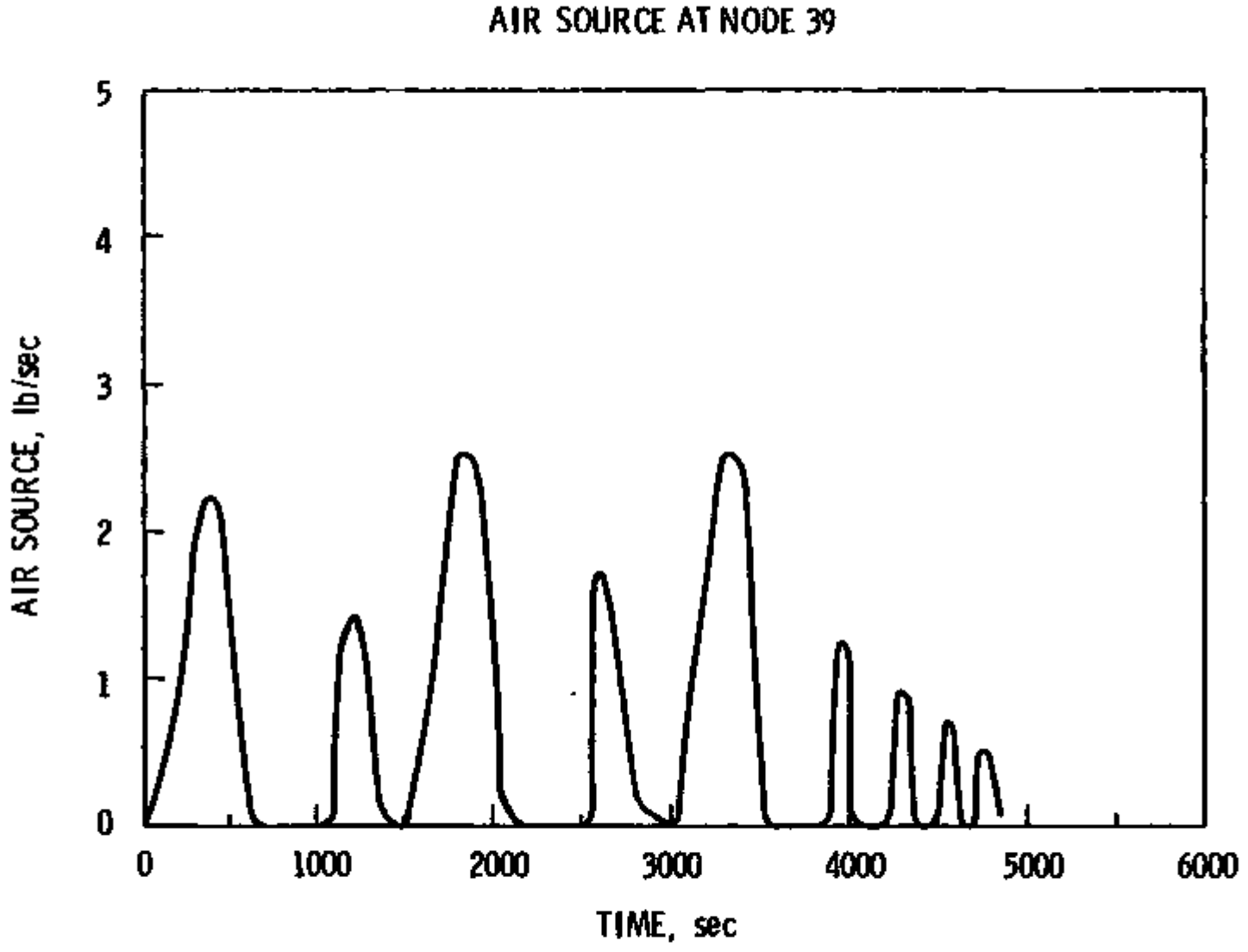


Figure VI-4. Air Source at Node 39.

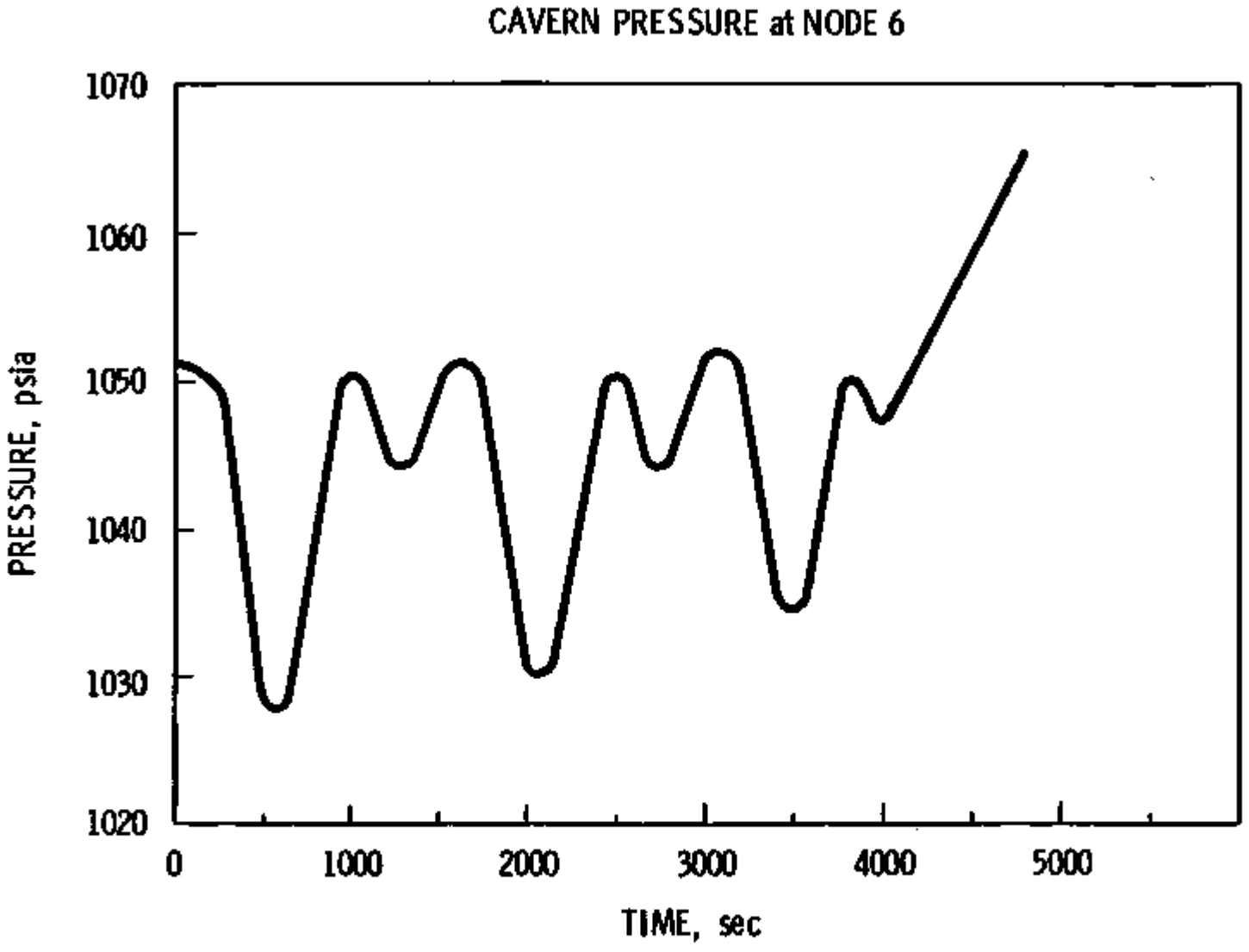


Figure VI-5. Cavern Pressure at Node 6.

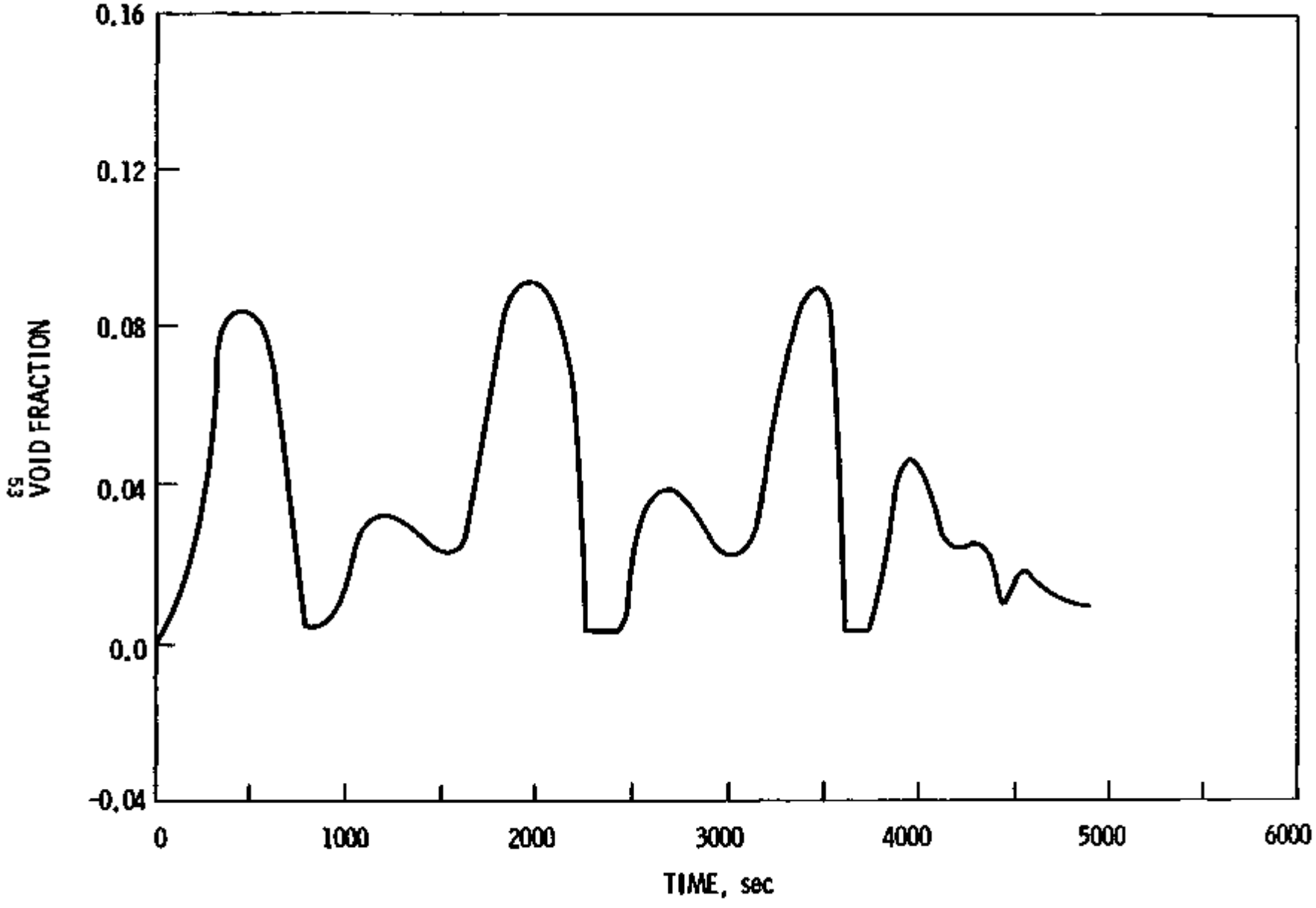


Figure V1-6. Void Fraction at Node 39.

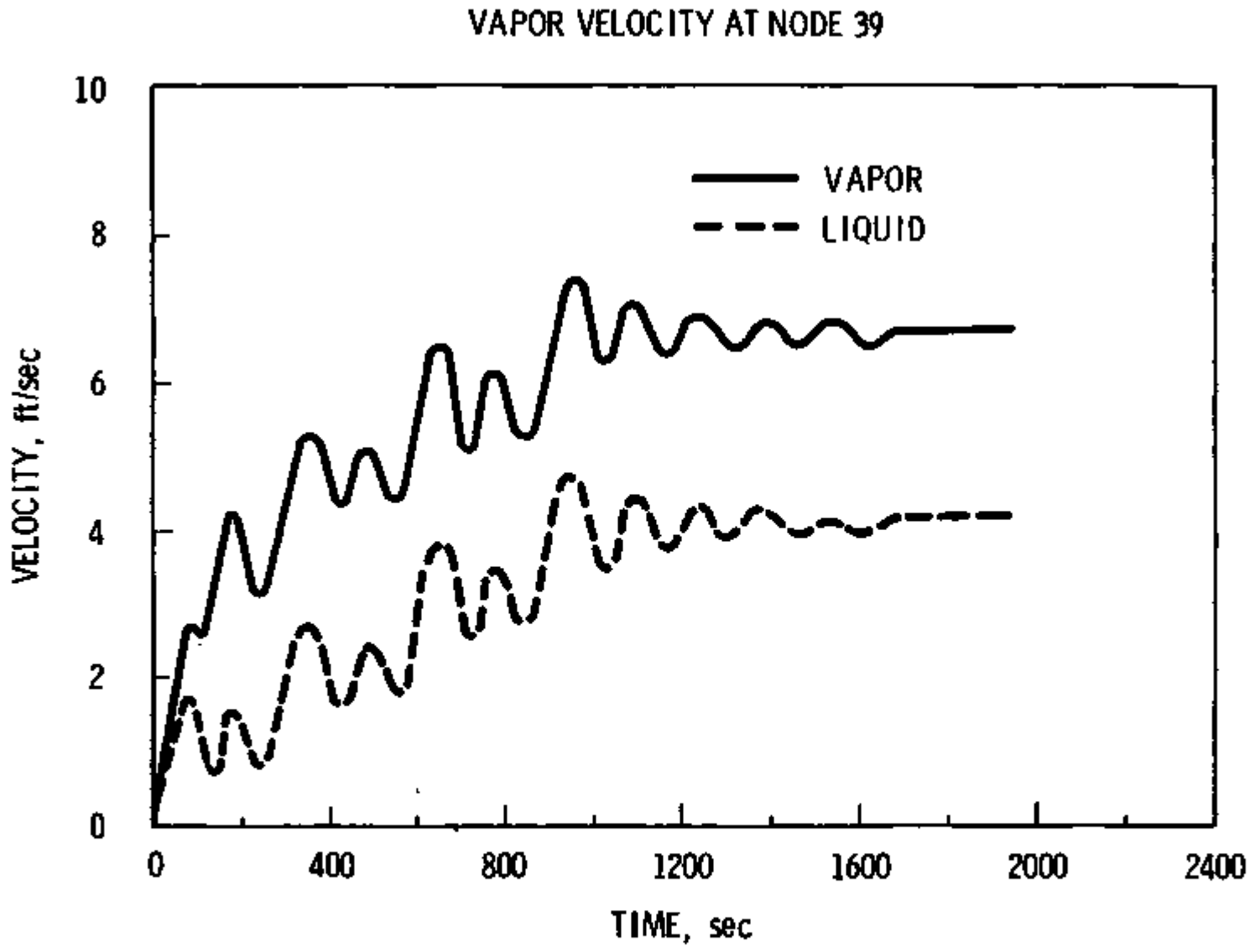


Figure VI-7. Velocity at Node 39.

## Section VII

## REFERENCES


1. J. C. Mollendorf, "Champagne Effect Phenomena in Hydraulically-Compensated Compressed-Air Energy Storage Systems", (Report to Acres American).

2. W. A. Blecher, A. J. Giramonti, and E. B. Smith, "The Champagne Effect in Hydraulically Compensated Compressed Air Energy Storage Systems", (United Technologies Research Center, East Hartford, CN).

3. F. H. Harlow and A. A. Amsden, "A Numerical Fluid Dynamic Method for All Flow Speeds", Journal of Computational Physics, Vol. 8, 1971, pp. 197-213.

4. "Transient Reactor Analysis Code (TRAC-PIA)", Los Alamos Scientific Laboratory, Los Alamos, NM.

5. M. Ishii, Thermo-Fluid Dynamic Theory of Two-Phase Flow, Eyrolles, Paris, 1975.

6. Perry, Editor, Chemical Engineer's Handbook, 5th Ed., McGraw Hill.

7. W. A. Blecher (UTRL), Personal Communication, December 14, 1979.

8. J. Pellen, (SEO, Luxembourg), Presentation at DOE/EPRI Meeting, December 14, 1979, Washington D.C.

9. I. Larsen and D. Noren, "Hydraulics of Compressed Air Power Plants", III Conference on Compressed Gas Economy, Budapest, April 1973.

10. M. Ishii and T. C. Chawla, "Two-Fluid Model and Momentum Interaction Between Phases," NRC Seventh Water Reactor Safety Research Information Meeting, November 1979, Gaithersberg, MD.

## Section VIII

## Appendix: HCAESS Computer Program Description and User Instructions

The calculations described in the body of this report were performed with the HCAESS (Hydraulically Compensated Compressed Air Energy Storage Simulation) computer program. The purpose of this appendix is to describe the structure of the CAESS computer program and to detail input data required for problem simulation.

### SUBROUTINE STRUCTURE AND DESCRIPTION

Figure A-1 shows the computer program subroutine structure. A brief summary of each subroutine follows.

PROGRAM HCAESS-

HCAESS is the executive routine which directs the overall sequence of events leading to the problem solution.

SUBROUTINE SETUP-

All problem initialization is accomplished in this subroutine. Required inputs to the mathematical model are summarized below:

- Geometry and Nodalization
- Equations of State
- Boundary Conditions
- Initial Conditions
- Correlation
  - Wall Friction
  - Interfacial Friction
  - Air Source

Details of input requirements are contained in the following section of the appendix.

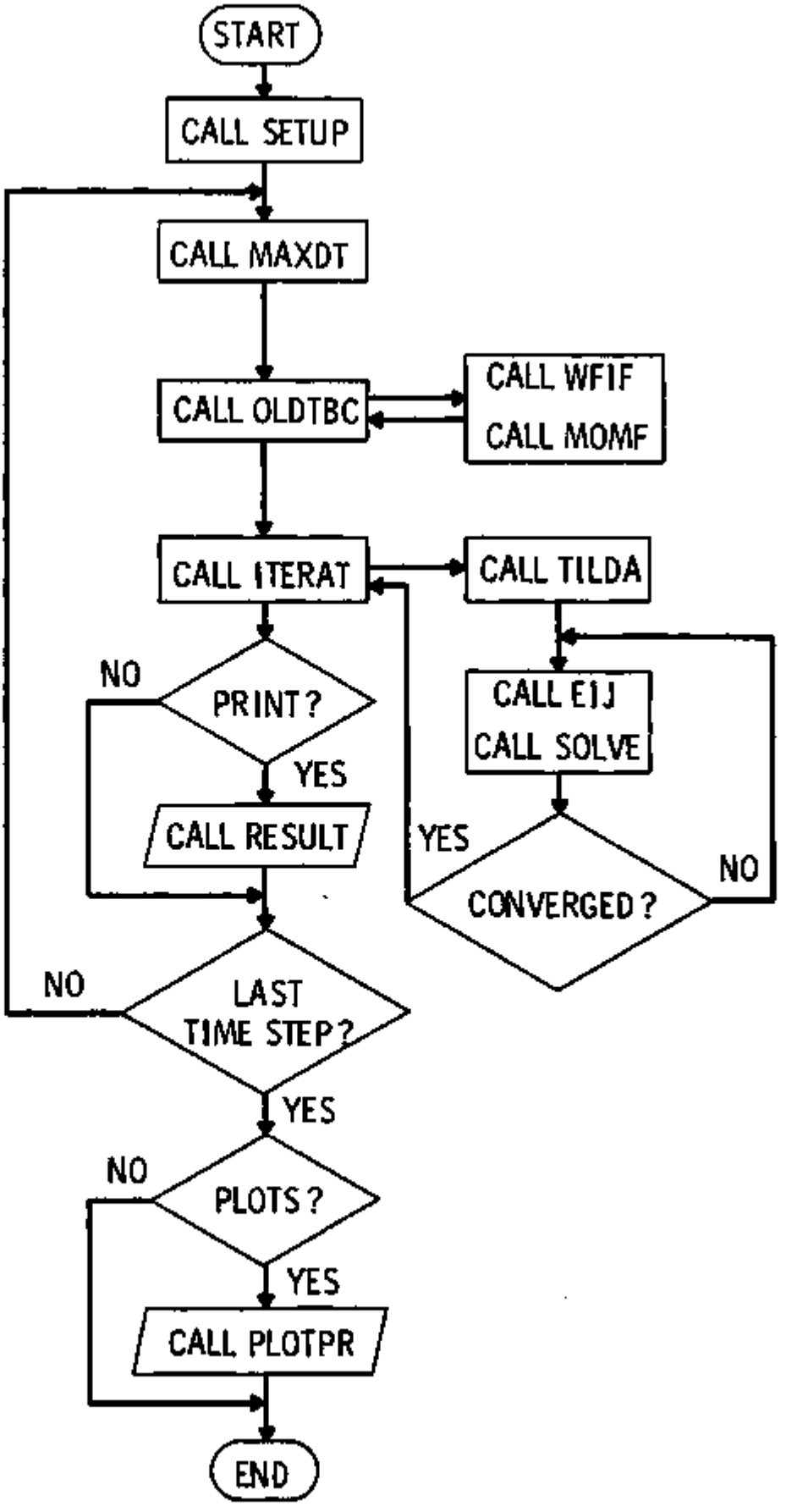


Figure A-1. Flow Diagram for Main Program-HCAESS

SUBROUTINE MAXDT -

The maximum permissible time step size is determined in this subroutine based on user selected values of Courant number and maximum desired time step.

SUBROUTINE OLDTBC -

This subroutine sets old time variables and new time boundary conditions. OLDTBC calls two other subroutines. The first is WFIF which calculates wall and interfacial friction factors, and the second is MOMF which calculates the explicit momentum flux terms.

SUBROUTINE ITERATE -

Subroutine ITERATE controls the iterative solution for a specific time step. ITERATE calls three other subroutines. The first is TILDA which calculates the coefficients of the liquid and vapor momentum equations depending on old time quantities and then sets the tilda flows based on these newly evaluated coefficients and the presently known pressures.

An iterative do loop is then entered. ITERATE calls Subroutine EIJ which evaluates the error in the volumetric form of the mixture mass conservation equations and determines the derivative of the error equation with pressure. ITERATE next calls SOLVE which determines the pressure adjustments and updates all dependent variables.

The iteration procedure continues until the user-supplied convergence criteria is satisfied or the user-supplied maximum number of iterations are performed.

SUBROUTINE RESULT -

Calculated results are output from this subroutine.

## DATA INPUT

Code initialization is set by data statements in Subroutine Setup to establish geometry, physical properties, friction correlations, initial conditions, boundary conditions, calculational parameters and printer

plot information. A general description of code input and a specific example for the sample problem provided with the code are discussed in this section of the report.

Before proceeding with the detailed data description, the user should be familiar with the general approach used to describe a particular problem. The first step is to assure familiarity with the positions at which variables are defined. Figure A-2 reviews variable placement on the calculational grid and shows two momentum cells (bounded by pressure $P_1$ and $P_2$, and by $P_2$ and $P_3$) and one continuity cell (bounded by velocities $U_1$ and $U_2$). The geometry is defined by the area, $A_i$, at the momentum cell boundaries and by the distance between pressures. The area is assumed to vary linearily over DX if the bounding areas are not equal. Continuity cell boundaries are defined midway between momentum cell boundaries, and fluid properties: $\alpha$ , $\rho_1$ , $\rho_g$ , and $\rho_a$ ; are assumed constant within a continuity cell.

The second step in problem setup is to draw a picture of the air pipe, cavern, compensation pipe and reservoir, and determine the nodalization. Figure A-3 depicts nodalization of the sample problem provided in the code which is used as an example for the input data description. The nodalization shown represents continuity-cell boundaries. The relatively fine nodalization in the cavern and lower well is used to provide detail of the mixture level as the liquid level receeds into the well, and that near the reservoir and top of the compensation pipe is used to assure detail where the air dissolution process is most significant. Relatively coarse nodalization is used in regions such as the air shaft where detail is not required. It is important to note that the first and last cells are used for boundary condition information only; results are not calculated for these positions.

Code input is described in general by input group and specifically for the sample problem in the following discussion.

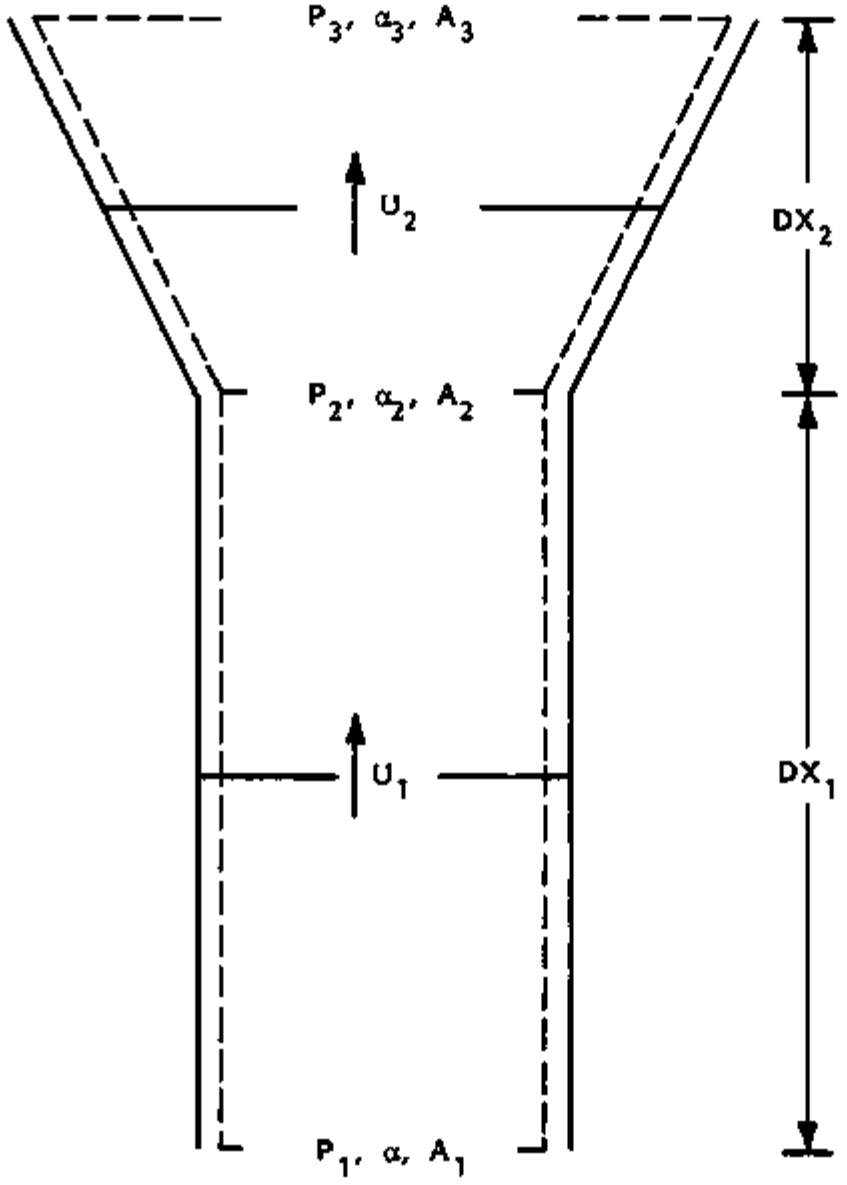


Figure A-2. Variable Placement on the Calculational Grid.

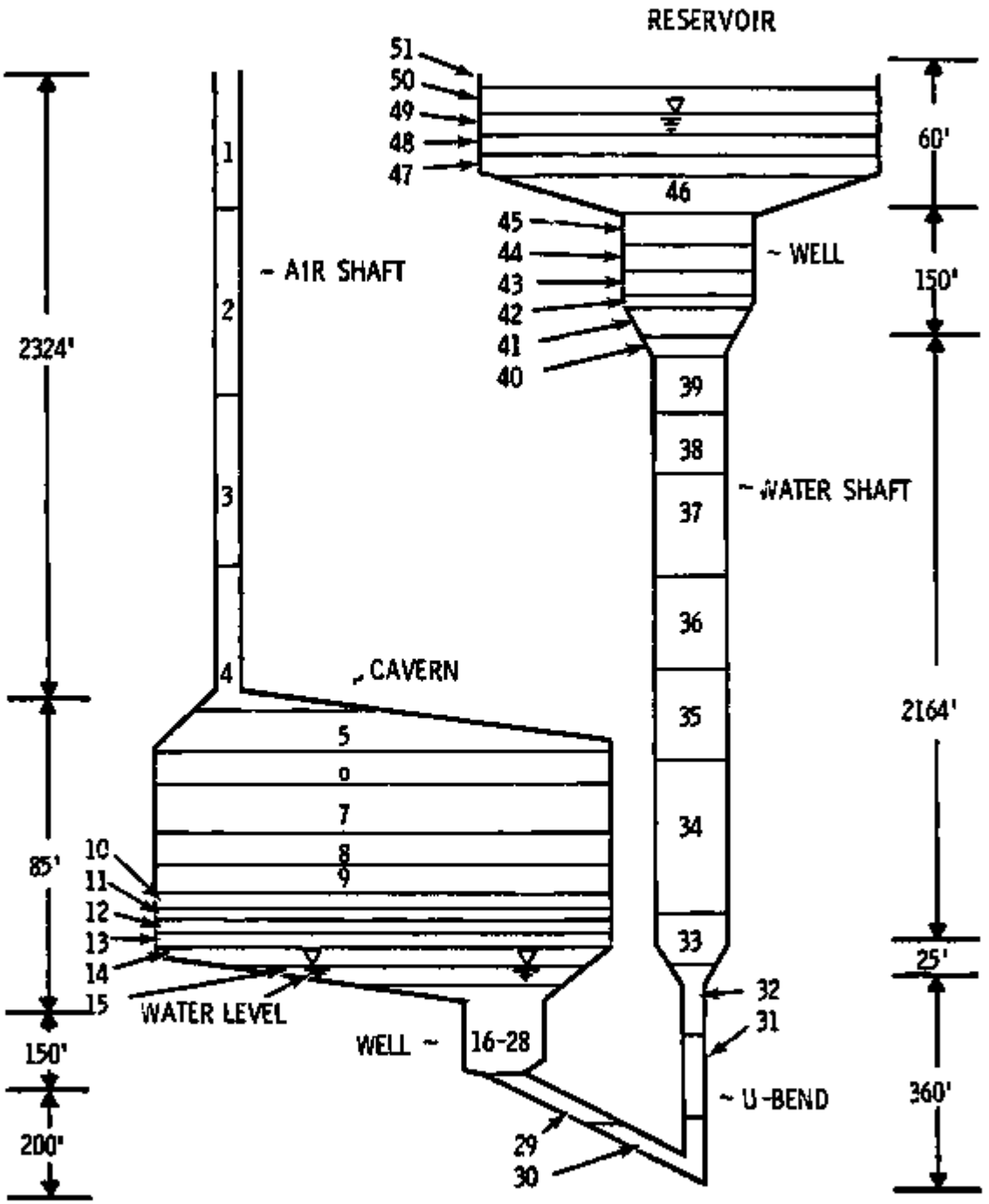


Figure A-3. System Nodalization.

TITLE

The problem title is input using a Hollerith format and may be up to 50 characters in length. See the sample problem input, Figure A-4, as an example.

NODE NUMBERS

Node numbers, ITYP(I), are input for every node for which input data will be entered. Data may be entered for every node or, if several nodes are the same, repetative data may not be required. Numbering must be ordered from high to low, beginning with the highest cell. The last entry must be a 0. For example, assume a problem with 10 nodes. Three permissible inputs are:

```
DATA ITYP  / 10,9,8,7,6,5,4,3,2,1,0 /
DATA ITYP  /-10/
DATA ITYP  / 10,5,4,1,0 /
```

The first statement specifies that node dependent data (areas, etc.) will be entered for every node. The second entry, negative the highest node number, is another way to specify that data will be entered for every node. The third statement specifies that node dependent data will be entered only for Nodes 10, 5, 4 and 1. Data for nodes not specified are assumed to be same as those for the next highest numbered node for which data is input. Therefore, in the third example, data for Nodes 9, 8, 7 and 6 are the same as those for Node 10; and data for Nodes 3 and 2 are the same as those for Node 4.

In the sample problem, data is entered for 24 nodes out of a total number of 51.

GEOMETRY

Required geometric data are ATYP(I), DXTYP(I) and GTYP(I) for every node specified by ITYP(I). These data must be input in the same order as the node numbers.

```
C
C     INPUT DATA STATEMENTS
C
C     **********
C     **********
C     TITLE
C     **********
      DATA TITLE /8HSAMPLE P,8HROBLEM   /
C     **********
C     NODE NUMBERS FOR WHICH DATA IS ENTERED
C     **********
      DATA ITYP /51, 19, 46, 45, 40, 39, 37, 32, 31, 29,
     $  28,  27,  15,  14,  13,  12,  9,  8,  7,  6,
     $  5,  4,  3,1,0/
C     **********
C     GEOMETRY
C     **********
      DATA DXTYP / 8.,   8., 20.,  30.,  10.,  45.,  416.8,  25.,
     $  180.,283.14,
     $ 20.,8.333,  3.,  4.,  3.,  3.,  3.,  3., 27., 27., 4.,
     $ 2.,929.6,  929.6 /
      DATA ATYP/ 2*.709E6,2*1963.5,  3*132.7,  3*50.26,
     $  2*1963.5, 9*.2526E6,3*12.57/
      DATA GTYP/  9*(-1.),  .8158,  14*1./
C     **********
C     PROPERTIES
C     **********
      DATA RV1ATM,RHOF,VAVH /.0763,62.3,6.38E-6/
      DATA VISL,VISV,SIGMA /7.53E-4,1.19E-5,4.98E-3/
      DATA HEN0,HEN1,XMGAS,XMLIQ /6.2E4,433.8,28.97,18.0/
C     **********
C     INTERFACIAL FRICTION PARAMETRERS
C     **********
      DATA CRITEB,DBMAX,CB1,CB2,CB3,CB4  /25.,.4,240.,24.,18.7,.68/
      DATA CZERO1,CZERO2 /1.0,0.0/
C     **********
C     WALL FRICTION COEFFICIENTS
C     **********
      DATA ALAM,ATUR,BTUR,CTUR,DTUR /64.,.316,0.,-.25,.015/
C     **********
C     LOSS COEFFICIENTS
C     **********
      DATA COETYP /40*0./
C     **********
C     INITIAL CONDITIONS
C     **********
```

Figure A-4. Sample Problem Data Statements.

```
      DATA ALTYP /1.,1940.,4*1./
      DATA IAIR /11/
      DATA PTOP /2116.8/
C     **********
C     TRANSIENT BOUNDARY CONDITIONS
C     **********
      DATA COMPF,RAMP,OFF,T1,T2,T3,T4 / 660.,15.,5000.,0.,300.,600.,
     $  900./
C     **********
C     CALCULATIONAL AND OUTPUT PARAMETERS
C     **********
      DATA COURM,DELTAT,ECONV,MAXIT /.5,.5,5.E-6,7/
      DATA COURM,DELTAT,ECONV,MAXIT /.5,2.,5.E-6,7/
      DATA NODT,NPRINT,XMAXT/ 200,3000,2000./
C     **********
C     PRINTER PLOT SPECIFICATION
C
C     WARNING, WRITE STATEMENTS IN THE MAIN PROGRAM MUST BE
C     CONSISTENT WITH PRINTER PLOT INPUT DATA
C     **********
      DATA ALLTIT /
     $  "TIME SEC","          ","          ","          "
     $,"VFLX 39  ","          ","          ","          "
     $,"VFLX 1   ","          ","          ","          "
     $,"AL 39    ","          ","          ","          "
     $," P 6     ","          ","          ","          "
     $,"UV 39    ","          ","          ","          "
     $,"UL 39    ","          ","          ","          "
     $,"SAIR 39  ","          ","          ","          "
     $/
      DATA IPLTQ /2,3,4,5,6,7,8,0/
C
C
```

Figure A-4 (continuted). Sample Problem Data Statements.

ATYP(I) - Flow area, $ft^2$. ATYP is defined at the boundaries of the momentum computational cell (see Figure A-2).

DXTYP(I) - Distance, ft, between boundaries of the momentum computational cell (see Figure A-2).

GTYP(I) - Gravitational factor, dimensionless. The gravitational force over the momentum computational cell is defined as g = GTYP*(32.2 $ft/sec^2$). GTYP is defined as negative cosine of the cell orientation where 0° is defined for a vertical cell with positive (from node i to i+1) flow upward. For example, GTYP equals -1. if the node is vertical and positive flow is upward, and GTYP equals 1.0 if the node is vertical and positive flow is downward.

The geometry input section for the sample problem, Figure A-4, illustrates geometrical input via Data Statements. Data is input for every node defined by ITYP. Note also the shorthand input method possible with Data Statements (integer constant*value) where, for example, DATA DUMY/3*.04/ is the same as DATA DUMY/.04,.04,.04/

PROPERTIES

RV1ATM - Vapor density, $lbm/ft^3$, for air at 14.7 psia and the user determined reference temperature. Perfect gas behavior is assumed for the vapor, therefore,
$\rho_g = P \cdot RV1ATM/(14.7\ psia)$

RHOF - Liquid density, $lbm/ft^3$, at the user determined reference temperature. Liquid density is assumed to be independent of pressure.

HEN0, HEN1, XMGAS, XMLIQ - Coefficients used in the determination of $\rho_{asat}$.

$$\rho_{asat} = \frac{\rho}{(HEN0+HEN1*(P-1))} \frac{XMGAS}{XMLIQ} \rho_1$$

Compare to Equation (3.13).

VISL - Liquid viscosity, lbm/(sec-ft)

VISV - Vapor viscosity, lbm/(sec-ft)

SIGMA - Surface tension, lbf/ft

INTERFACIAL FRICTION PARAMETERS

CRTWEB - Critical Weber number for bubbles, dimensionless.

DBMAX - Maximum bubble diameter, ft.

CB1,CB2 CB3,CB4 - Coefficients used to determine the interfacial drag coefficient, CB, in conjunction with the bubble Reynolds number, $Re_b$, such that,

$Re_b \leq .1$, CB=CB1

$.1 < Re_b \leq 2.0$, $CB = CB2/Re_b$

$2.0 < Re_b$, $CB = CB3/Re_b$

CZERO1, CZERO2 - Coefficients used to determine $C_o$, the distribution parameter: $C_o = CZERO1 - CZERO2*(\rho g/\rho l)^{.5}$

WALL FRICTION

The wall friction factor is defined as the maximum of the laminar and turbulent values as evaluated by the mixture Reynolds number, $Re_m$.

ALAM - used to evaluate $f_{lam} = ALAM/Re_m$

ATUR, BTUR, CTUR, DTUR - Coefficients used to evaluate the turbulent friction factor $f_t$ where,

$f_t = \text{maximum } (ATUR*Re_m^{CTUR}+BTUR, DTUR)$

LOSS COEFFICIENTS

COETYP(I) - loss coefficient defined for the node number, ITYP.

Sample input for properties and friction factors is illustrated for the sample problem in Figure A-4.

INITIAL CONDITIONS

ALTYP, IAIR and PTOP are required initial conditions. Initial flows are assumed to be zero.

ALTYP(I) - Nodal void fractions defined for the node numbers ITYP(I).

IAIR - Initial values of $\rho_a$ are set to the minimum of the saturation value at the cell pressure and $\rho a_{SAT}$ for the cell IAIR.

PTOP - Atmospheric pressure at the reservoir, $lbf/ft^2$.

TRANSIENT BOUNDARY CONDITIONS

The air-charging/discharge process is defined by following input parameters:

COMPF - Air flow rate, lbm/sec, of one compressor.

T1,T2 T3,T4 - Times, seconds, when compressors 1 through 4 start.

RAMP - Time, seconds, between compressor initiation and full flow.

OFF - Time, seconds, when all compressor flow stops.

CALCULATIONAL PARAMETERS

COURM - Courant number, $\frac{U\Delta t}{\Delta x}$, used to determine the maximum allowable $\Delta t$. $0. < COURM < 1.$

DELTAT - Maximum $\Delta t$ regardless of that calculated from COURM.

ECONV - Convergence criteria,

$$\frac{\text{node liquid mass error/second}}{\rho_l V_c} + \frac{\text{vapor mass error/second}}{\rho_g V_c}$$

or, $$\frac{\%\text{continuity error}}{100 \text{ seconds}}$$

The solution will iterate until the maximum error in any node is less than ECONV, but is required to iterate at least 2 times and will iterate a maximum of MAXIT (defined below) times.

MAXIT - Maximum number of iterations allowed at any one time step for convergence.

NODT - Maximum number of time steps.

NPRINT - Results are printed every NPRINT time steps.

XMAXT - Maximum total time for the calculation.

PRINTER PLOT SPECIFICATIONS

Selected variables are written to TAPE17 every time step, or at equal intervals up to 75 times during the calculation, for use by the printer plot routine at the end of the calculation. Two actions are required to obtain printer plots. The first is to change the coding in the main program so that the appropriate variables are written to TAPE17 during the calculation. Of these, the first value written must be the time. Figure A-5 is a listing of the variables output in the sample problem to provide an illustration of how this is done. The second step is to set the following data:

ALLTIT - Hollerith data describing the variables written in the main program. For example, as shown in Figure A-4, the first title is TIME SEC which is used to describe the first variable written, TIME.

IPLTQ(I) - An integer array whose numbers indicate variables to be plotted as a function of time. The last entry must be 0. For example, DATA IPLTQ/5,6,0/ directs plotting the fifth and sixth variables written from the main program. Recall that time is the first variable.

```
PLTARY(1) = TIME
JDV = JSTV(2,39)
JDL = JSTL(2,39)
JDV = 1
JDL = 1
PLTARY(3) = VFLX(2,1)
PLTARY(4) = AL(2,39)
PLTARY(5) = P(2,6)/144.
PLTARY(6) = RAIR(2,39)
PLTARY(7) = UV(2,39)
PLTARY(8) = UL(2,39)
PLTARY(9) = SAIR(2,39)
```

Figure A-5. Plot Variable Outputs From the Main Program Used in the Same Problem.

# DISTRIBUTION

No of Copies

OFFSITE

US Department of Energy
Attn: J. Brogan
Office of Energy Systems Res.
Forrestal Building
1000 Independence Ave., S.W.
Washington, DC 20585

US Department of Energy
Attn: R. A. Dunlop
Div. of Electric Energy Sys.
12 & Pennsylvania
Washington, DC 20585

US Department of Energy
Attn: I. Gyuk
Office of Energy Systems Res.
Forrestal Building
1000 Independence Ave., S.W.
Washington, DC 20585

US Department of Energy
Attn: R. Shivers
Office of Energy Systems Res.
Forrestal Building
1000 Independence Ave., S.W.
Washington, DC 20585

US Department of Energy
Attn: J. H. Swisher
Office of Energy Systems Res.
Forrestal Building
1000 Independence Ave., S.W.
Washington, DC 20585

27 DOE Technical Information Center

Acres American, Inc.
Attn: C. Driggs
The Clark Building
Suite 329
Columbia, MD 21044

No of Copies

Acres American, Inc.
Attn: D. Willett
Liberty Bank Building
Main at Court
Buffalo, NY 14202

Central Illinois Public Service Co.
Attn: A. H. Warnke
Vice President Power Supply
607 East Adams Street
Springfield, IL 62701

Commonwealth Edison Co.
Attn: T. J. Maiman
Sta. Mech. Engr. Dept. Mgr.
36 FN West
PO Box 767
Chicago, IL 60690

Electric Power Research Inst.
Attn: R. B. Schainker
3412 Hillview Avenue
PO Box 10412
Palo Alto, CA 94303

Harza Engineering Co.
Attn: A. H. Barber
Director of Marketing
150 S. Wacker Drive
Chicago, IL 60606

Illinois Power Company
Attn: G. E. Huck
Manager of Planning
500 South 27th St.
Decatur, IL 62525

Lawrence Livermore Laboratory
Attn: Jesse Yow
PO Box 808
Mail Stop L-202
Livermore, CA 94550

No of
Copies

Lawrence Livermore Laboratory
Attn: Tech. Info. Dept, L-3
University of California
PO Box 808
Livermore, CA 94550

Middle South Services
Attn: L. A. Wilson
Advanced Energy Program
Section
Box 6100
New Orleans, LA 70161

Northern Research & Eng. Corp
Attn: Jerry O. Melconian
39 Olympia Avenue
Woburn, MA 01801

Potomac Electric Power Co.
Attn: P. E. Schaub
1900 Pennsylvania Ave
Washington, DC 20006

Public Service of Indiana
Attn: T. W. McCafferty
1000 E. Main Street
Plainfield, IN 46168

5 Rowe and Associates
Attn: D. Rowe
14400 Bellevue-Redmond Road
Suite 208
Bellevue, WA 98007

Sandia Laboratories
Attn: William G. Wilson
PO Box 969
Organization 8453
Livermore, CA 94550

Sandia Laboratories
Attn: R. O. Woods
Organization 4715
Albuquerque, NM 87115

No of
Copies

Sargent and Lundy Engineers
Attn: W. C. Walke
Project Manager
55 East Monroe Street
Chicago, IL 60603

Soyland Power Cooperative,
Inc.
Attn: R. Ruzich
PO Box A1606
Decatur, IL 62525

Tennessee Valley Authority
Attn: A. Betbeze
1150 Chustnut, Tower 2
Chattanooga, TN 37401

Tennessee Valley Authority
Energy Research Section
1360 Commerce Union Bank
Bldg.
Chattanooga, TN 37401

TRW Energy Systems Group
Attn: E. Berman
Technical Library
7600 Colshire Drive
McLean, VA 22101

Union Electric Co.
Attn: E. M. Mabuce
Manager - Applied Research
Corporate Planning Dept.
PO Box 149
St. Louis, MO 63166

United Engineers & Constructors
Attn E. Sosnowicz
Advanced Eng. Dept. 04U3
30 South 17th
Philadelphia, PA 19101

United Technologies Research
Center
Attn: A. J. Giramonti
Silver Lane
East Hartford, CT 06108

No of
Copies

University of Massachusetts
Attn: O. C. Farquhar
Dept. of Geology & Geography
Morrill Science Center
Amherst, MA 01003

University of Michigan
Attn: Donald L. Katz
Dept. of Chemical Eng.
2042 E. Engr. Bldg.
Ann Arborn MI 48109

Westinghouse Electric Corp.
Attn: D. L. Ayers
Fluid Systems Laboratory
1291 Cumberland Avenue
West Lafayette, IN 47906

Westinghouse Electric Corp.
Attn: W. F. Kobett
CAES Project Manager
Combustion Turbine Sys. Div.
Long Range Develop-Lab 100
PO Box 251
Concordville, PA 19331

FOREIGN

Central Electricity Generating
Board
Attn: I. Glendenning
6 Georgian Close
Gloucester England
9L4 9DG

ONSITE

DOE Richland Operations Office

H.E. Ransom/D.R. Segna

Pacific Northwest Laboratory

L.D. Kannberg (15)
Technical Information (5)
Publishing Coordination (2)